RICE UNIVERSITY

By

Haad Y Rathore

A THESIS SUBMITTED
IN PARTIAL FULFILLMENT OF THE
REQUIREMENTS FOR THE DEGREE

Master of Science

APPROVED, THESIS COMMITTEE

Barry Dunning
Barry Dunning (May 17, 2020)
F. Barry Dunning

Chong Xie
Chong Xie

Thomas Killian
Thomas Killian (May 17, 2020)
Thomas Killian

Kevin F. Kelly
Kevin F. Kelly (May 17, 2020)
Kevin Kelly

HOUSTON, TEXAS
May 2020

Contents

Abstract

In this work we describe the design and implementation of an optical system that enables the study of the interactions of Rydberg atoms or other Rydberg species in well-defined geometries. To understand and observe the dynamics of Rydberg interactions, the ability to engineer different arrangements of microscopic cold atom traps and manipulate their positions with a precision of a few microns is essential. This is accomplished by a custom designed high-numerical-aperture long-working-distance objective lens and a spatial light modulator device to control the phase of an incoming optical beam. Several different trap geometries have been realized, with a spatial resolution of a few microns, including a 1-dimensional chain, a 2-dimensional square grid, and a circular array of traps. The objective lens has been designed to provide diffraction limited performance at multiple wavelengths facilitating the creation of not only micron-scale atom traps but also the fluorescence imaging of trapped atoms. The system enables precise control over trap positions, and hence the locations at which atoms might be excited, with applications in, for example, the study of long-range interactions between Rydberg atoms, the creation of long-range Rydberg molecules, the implementation of qubits for quantum computing based on Rydberg atoms, and in quantum simulation.

Chapter 1

Introduction

1.1 Background and Motivation

An atom with at least one electron in a highly excited quantum state, generally with principal quantum number $n > 30$ is termed as a Rydberg atom. The study of Rydberg atoms is an active area of research in ultracold atomic physics and such species have been used in areas as diverse as quantum information [1], quantum computation [2], the formation of ultralong-range Rydberg molecules [3] and the investigation of quantum critical behavior [4]. The fact that they have extremely long lifetimes and properties that can be tuned over many orders of magnitude has made Rydberg atoms attractive as a model system for studying quantum physics [5–7]. Rydberg atoms possess exaggerated properties because the valence electron is far away from the inner shell electrons as well as the core ion. For example, the polarizability of a

Rydberg atom scales with n^7 while the van der Waals force between Rydberg atoms scales as n^{11}. Due to these enhanced properties, Rydberg atoms are particularly useful to study and simulate many-body interactions important in condensed matter physics. The strength of their dipole-dipole interactions can be manipulated by selecting specific (n, l) Rydberg states as well as by controlling the spatial distance between two (or more) Rydberg atoms. For example, to increase the interaction strength, a state with a larger quantum number n can be excited. The energy levels and transitions important in the present work are shown in the atomic energy level diagram for Strontium (Sr) presented in Figure 1.1.

Rydberg atoms can be created at a precise point in space by using a highly focused laser beam to create localized Optical Dipole Traps (ODTs) in which ground-state atoms are tapped prior to their excitation. In this thesis, we describe the design and implementation of an optical system that employs a Spatial Light Modulator (SLM) that is capable of creating arbitrary ODT configurations with the goal of controlling the interactions between two (or more) Rydberg atoms at length scales of a few microns to tens of microns. The theory behind generating the different trapping geometries will be described together with the creation of tightly focused single ODTs, 1D and 2D arrays of traps and, finally a ring lattice of ODTs.

The creation of a single Rydberg atom in a trap will rely upon the Rydberg blockade effect, which allows only one atom to be excited to a Rydberg state within a certain volume. The region surrounding this Rydberg atom

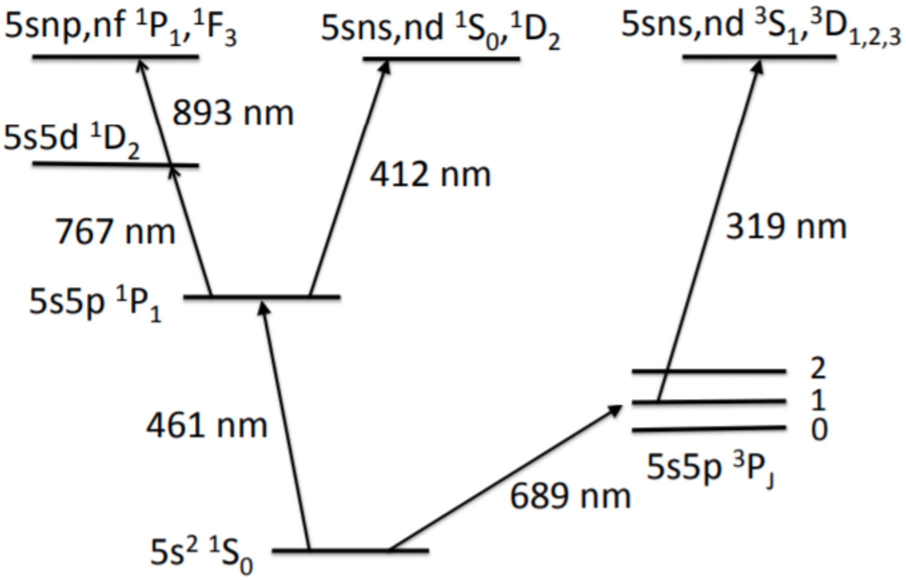

Figure 1.1: A section of the Strontium energy level diagram showing the relevant transitions to excite ground state atoms to Rydberg states using various optical wavelengths. The energy level diagram shows two-photon as well as three-photon excitations for various final Rydberg states. The main fluorescence transition at $461\,nm$ is also shown. This transition, along with the $689\,nm$ transition, is also used for cooling the atoms in the Magneto-Optical Trap (MOT). [8]

is known as the blockade volume and can be understood as follows. In the vicinity of a single Rydberg atom, other Rydberg atoms experience a strong potential due to the dipole-dipole interaction which causes their energy levels to shift. This shift in the energy levels depends on the quantum numbers *(n,l)* of the Rydberg states as well as the spatial distance between the two atoms. Thus, neighbouring atoms are no longer in resonance with the Rydberg excitation light and are not excited to the Rydberg state whereupon only a single Rydberg atom can be excited in a tightly localised ODT. For further details about the properties of Rydberg atoms, the interested reader is referred to [9, 10].

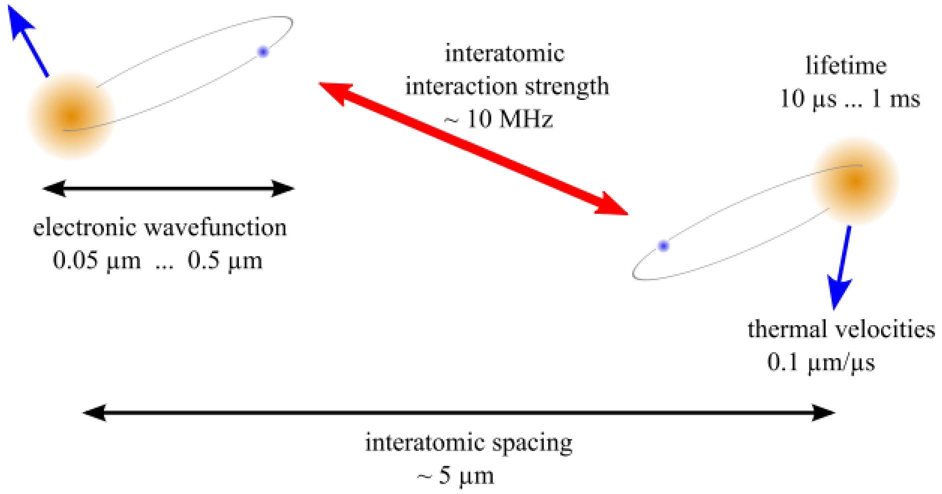

Figure 1.2: The figure shows typical parameters for Rydbergs atom created in a MOT. Strong interactions on the order of a few MHz are present over interatomic distances of a few microns. [11]

The trapping and cooling of Sr utilizes powerful techniques that have been developed over the last 30 years [12, 13]. First, a Sr oven operating around 700 K (425°C) is used to vaporize a sample of metallic Sr. It is followed by a 2D optical molasses to collimate and shape the atomic beam. The resulting atomic beam is collected and cooled to mK temperatures by using a Zeeman slower opening up to the 3D Magneto-Optical-Trap (MOT). The Zeeman slower uses the $(5s^2)\ ^1S_0$ - $(5s5p)\ ^1P_1$ transition which is also called the blue (461 nm) transition. The current setup employs two MOTs: i) Blue MOT operating on the same broad linewidth 461 nm transition as mentioned above and ii) Red MOT operating on the narrow linewidth $(5s^2)\ ^1S_0$ - $(5s5p)\ ^3P_1$ transition which results in further lowering of the temperature to the μK regime. This is also called the red (689 nm) transition. The peak density of the atomic cloud at the end of the red MOT cooling stage is of the order of $1\text{x}10^{12}\text{cm}^{-3}$.

As mentioned previously, the valence electron of an atom in a Rydberg state is far away from the inner shell electrons as well as the positively charged core. For a Rydberg atom, this large distance results in their high polarizability. Thus, as expected, this results in a very large induced dipole moment in an external electric field which makes Rydberg atoms extremely sensitive to electric fields. This also enables us to probe long-ranged dipole-dipole and van der Waals interactions between atoms. This sets the interaction energy between neighbouring atoms in a MOT with mean interparticle distances of about 5 μm to be of the order of a few MHz.

In this thesis, I begin by introducing some basic theoretical framework by describing fluorescence imaging which is used to characterize local atom clouds by the process of light scattering, optical dipole trapping which enables us to localize a single or a bunch of atoms inside a small volume by using highly focused light beams, and finally aberration theory which proves to be extremely useful in designing a custom microscope objective to focus the beam. The thesis is divided into two main parts. In chapter 2, I describe the design, construction and testing of an optical system to generate extremely tight ODTs and manipulate their depth and position under computer control. In chapter 3, I talk about the design, construction and testing of a multi-element lens system by using the commercial ray-tracing software called OSLO Light. Finally, in chapter 4, the two projects are combined to build the final optical system for high-resolution imaging as well as high spatial resolution trapping of atoms in an ultracold atomic quantum gas.

1.2 Fluorescence Imaging

If a resonant (or nearly resonant) beam of light interacts with an atom, it can absorb photons from the light field and re-emit them via spontaneous emission with a decay constant characteristic of the particular transition. This scattering process between atoms and photons is called fluorescence and collecting this light using an objective lens and subsequently imaging onto a detector, constitutes fluorescence imaging. The resolution of the optical system is directly set by the Numerical Aperture (NA) of the objective which sets the light gathering ability of the imaging setup. The technique of fluorescence imaging is routinely used in ultracold atom experiments to measure the time of flight expansion of a cloud of gaseous atoms, to detect single ions in Paul traps [14], and single atoms in a dipole trap [15].

A major focus of this work was to develop a custom high resolution imaging system by considering the geometrical limitations of the vacuum chamber used in our experimental apparatus. Recent work in the laboratory has focused on creating Strontium Rydberg atoms and understanding the formation of long-range Rydberg molecules in an ultracold quantum gas. Rydberg atoms are highly suited to study long-range interactions since the van der Waals force between them is orders of magnitude stronger than between two ground-state atoms. This is particularly useful to study correlations in many-body systems. For example, high-resolution fluorescence imaging of ^{87}Rb Rydberg atoms has been used to directly study the strong correlations in a 2D Mott insulator where spatially ordered excitation patterns of well-defined geometry were observed [16].

The energy level diagram for Sr highlighting the states relevant to the present work is given in Figure 1.1. The $(5s^2)$ $^1S_0$ - $(5s5p)$ $^1P_1$ transition at $\lambda = 461$ nm is commonly used for fluorescence imaging and has a linewidth (FWHM) of 30.5 MHz. This transition is also used to create the standard six-beam "blue" MOT. The same high resolution imaging system can also be used to control the trapping potential on a microscopic scale (on the order of a wavelength of light) [17] by generating a tightly focused Gaussian beam in the center of the MOT or to create arbitrary trapping geometries as we shall explore in the next chapter.

1.3 Optical Dipole Trapping

There are two types of optical forces that can act on a single atom or an ensemble of atoms: the radiative force and the dipole force. The radiative force, which relies on the resonant or near-resonant interaction of an atom with the light field, serves as one of the essential components of the well known Magneto-Optical Trap (MOT) which has been used to confine a variety of atoms at mK and sub-mK temperatures [18, 19]. The dipole force on the other hand relies on the electric dipole interaction which causes a light shift in the atomic energy levels. We shall consider the far off resonant optical dipole trap at $\lambda = 532\, nm$ as used here which is far red detuned from the $^1P_1$ transition thereby ensuring that the probability of optical excitation is extremely low resulting in a low scattering rate. As shown below, the dipole force produced due to the spatial variation of the intensity of the light field results in a conservative potential.

An oscillating electric field of a monochromatic laser induces an oscillating atomic dipole moment in an atom that is proportional to the field strength

$$\boldsymbol{p} = \alpha(w)\boldsymbol{E} \tag{1.1}$$

where α is the complex polarizability and is a function of the optical frequency, w. The potential energy of an induced dipole in an electric field is given by

$$U_{dip} = -\frac{1}{2}\langle \boldsymbol{p} \cdot \boldsymbol{E} \rangle = \mathrm{Re}(\alpha)\boldsymbol{E}^2 \tag{1.2}$$

where the angular brackets represent the time average. Note that the intensity of the light field is defined as $I = 2\epsilon_0 c\boldsymbol{E}^2$. Thus the potential is proportional to the intensity of the light field. If we consider a two-level system, with energy splitting $\hbar w_0$, the sign of the detuning, $\Delta = w - w_0$, determines the sign of the polarizability. If $\Delta < 0$, the dipole potential for the ground-state atom is negative thus the dipole force, given by Equation (1.3), acts towards regions of high intensity. In other words, ground-state atoms are attracted towards the peak value of laser intensity. This is called a *red detuned* optical dipole trap (ODT).

$$\boldsymbol{F} = -\nabla U_{dip} \tag{1.3}$$

In contrast, if $\Delta > 0$, we are above resonance and the potential is positive everywhere whereupon atoms are then trapped in regions of lowest intensity. Laguerre-Gaussian beam modes [20, 21] are doughnut shaped beams with a node in the center, which, for *blue-detuned* light, have been demonstrated to trap ^{87}Rb atoms in their central dark region [22, 23]. This is advantageous because it results in a negligible scattering rate.

Since the dipole potential is proportional to the intensity of the light field, the shape of the potential seen by the atoms will correspond to the intensity profile of the laser. One of the major themes of this work is to shape the intensity distribution of a light beam, using the techniques of beam-shaping, to tailor the trapping potentials seen by the atoms.

The intensity distribution of a Gaussian beam of total power P, can be described mathematically as

$$I(r, z) = \frac{2P}{\pi w^2(z)} e^{-2\frac{r^2}{w^2(z)}} \tag{1.4}$$

where $w(z) = w_0\sqrt{1 + \left(\frac{z}{z_r}\right)^2}$ is the $\frac{1}{e^2}$ radius of the beam in the transverse plane, z_r is the Rayleigh range and w_0 is the minimum radius located at the waist. The trap depth is proportional to the peak intensity, $U(r = 0, z = 0) \propto I(r = 0, z = 0)$. An ODT created by a focused Gaussian beam provides tighter confinement in the radial direction as compared to the axial direction simply because of the intensity gradient is shallower along the direction of the beam, see Equation (1.4).

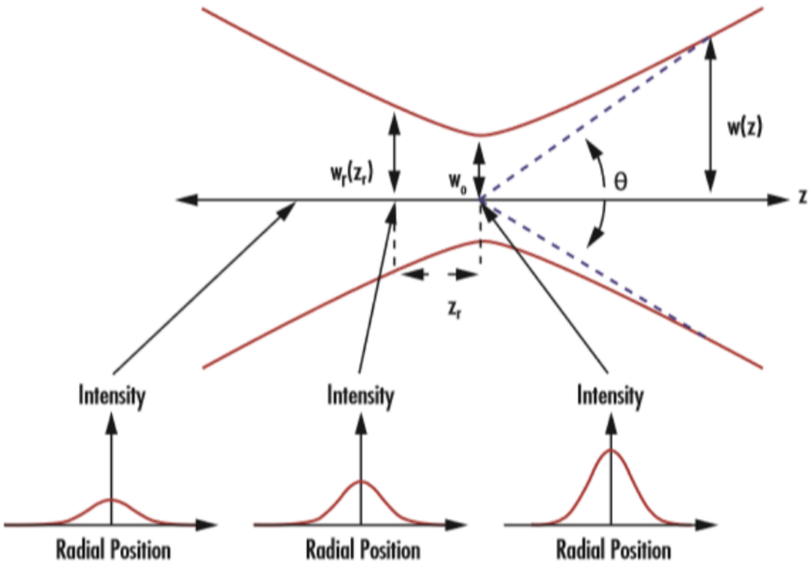

Figure 1.3: A Gaussian beam propagating along the z axis. The red line in the figure delineates the $\frac{1}{e^2}$ diameter along the beam propagation axis. The transverse (x, y) beam intensity profiles are shown, as a function of the radial coordinate, at three different slices. The intensity and the trapping potential are largest at the waist $(z = 0, r = 0)$.

For a two-level atom, with an excited-state decay rate Γ and energy splitting $\hbar w_0$, the complex polarizability α is given in the classical Lorentz spring model as

$$\alpha = 6\pi\epsilon_0 c^3 \frac{\Gamma/w_0^2}{w_0^2 - w^2 - i(w^3/w_0^2)\Gamma} \tag{1.5}$$

Substituting into Equation (1.2), we get

$$U(r,z) = \frac{Re(\alpha)}{2\epsilon_0 c} \frac{2P}{\pi w^2(z)} e^{-2\frac{r^2}{w^2(z)}} \tag{1.6}$$

For a red detuned ODT using a $\lambda = 532\,nm$ beam with $w = \frac{2\pi c}{\lambda}$, $w_0 = (2\pi)\,6.5\,\text{x}\,10^{14}$ Hz and $\Gamma = (2\pi)\,30.5\,\text{x}\,10^6\,s^{-1}$, the resulting trapping potential is shown in Figure 1.4.

1.4 Aberrations

Snell's Law, $n\sin(\theta) = n'\sin(\theta')$, relates the angle of incidence and the angle of reflection for a beam of light incident at the interface between two media. This relation is clearly non-linear but using the Taylor expansion, it can be linearized by writing $\sin(\theta)$ as

$$\sin(\theta) = \theta - \frac{\theta^3}{3!} + \frac{\theta^5}{5!} + ... \tag{1.7}$$

The paraxial approximation results when all the terms except for the first power in θ are discarded. Under this approximation, we can describe the theory of perfect image formation where all the rays from an object point converge to a single image point. We will explore this in chapter 3 where we describe the performance of a custom designed imaging lens under the

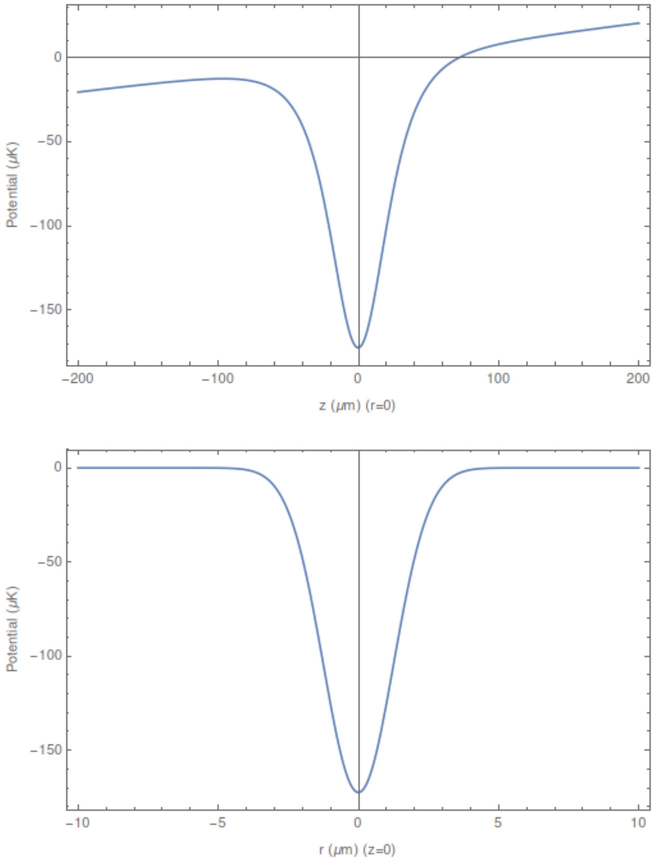

Figure 1.4: The potential as a function of the axial coordinate (top) and radial coordinate (bottom). The $1/e^2$ radius of the ODT is $w_0 = 2.5\,\mu m$ and the total power in the beam is $10\,mW$. The effect of gravity for ^{87}Sr is also included in the axial variation of the potential which causes the overall gradient in the curve (top). The trap depth is a little over $150\,\mu K$.

paraxial approximation. It is worth remembering that most of the results of geometrical optics which we are familiar with are only valid in the paraxial approximation which is sometimes called the small-angle approximation. If, instead, we keep terms up to the 3^{rd} order in θ, we are in the regime of Seidel aberrations[1] and if we keep terms upto the 5^{th} order, we are dealing with 5^{th} order theory of aberrations. Thus aberration theory simply expands upon the study of the errors introduced due to the paraxial approximation. The basic types of aberrations, shown in Figure 1.5, can be summarized as:

- **Tilt**: This is a 1^{st} order aberration and is caused due to a tilt between the actual wavefront and the reference wavefront. It can easily be corrected by changing the tilt angle of an optical system relative to the input ray fan.

- **Defocus**: This is also a 1^{st} order aberration and is caused by selecting an incorrect image plane thus blurring the image.

- **Astigmatism**: This is a 3^{rd} order aberration. A cylinderical deformation of the wavefront which would result in two line foci along two perpendicular planes.

- **Comatic Aberration**: This is a 3^{rd} order aberration. Causes a comet-like shape of an off-axis object point thus causing an asymmetry in the image. In other words, it causes a variation in the magnification in the transverse plane. It doesn't exist for on-axis object points.

---

[1] Also called 3^{rd} order aberrations

- **Spherical Aberration**: This is a 3^{rd} order aberration. Causes the optimal focal plane to deviate from the paraxial image plane. It increases with the height of the ray striking the lens and is the only aberration which exists for on-axis object points. It is responsible for the rotationally symmetric blurring of the image point.

- **Field Curvature and Distortion**: These two are 3^{rd} order aberrations. Both of these aberrations are only for off-axis object points. These do not effect the shape of the wavefront, which remains spherical, but instead are affected by the field position. They are relevant only for widely extended images with respect to the focal length, thus their effect will be minimal for our experimental purposes.

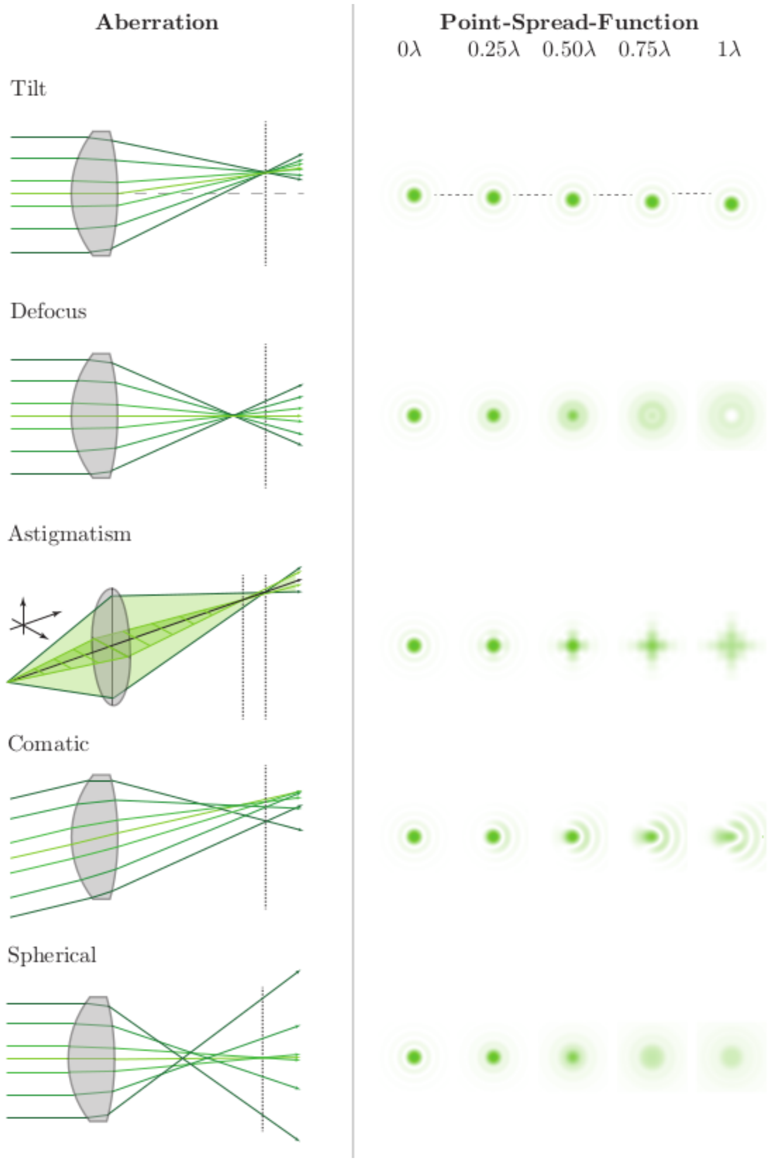

Figure 1.5: Visualizing the aberrations and showing the imperfections caused in the image of a single point like object. The effect of varying the peak-to-valley strength of the wavefront error on the resulting image profile is shown as well. [24]

Chapter 2

Optical Trapping System

2.1 The wave nature of light

Light can be described both classically and quantum mechanically and, depending on the application, one approach might be more useful than the other. For beam shaping applications, the wave theory of light is universally used, which under the scalar approximation assumes that the electric field of a monochromatic beam of light takes the form

$$u(\boldsymbol{r}, t) = A(x, y) \cos(2\pi v t - kz + \phi(x, y, t)) \tag{2.1}$$

where $u(\boldsymbol{r}, t)$ is the scalar electric field, at the position vector $\boldsymbol{r}$, of a plane wave travelling in the $\hat{\mathbf{z}}$ direction, v is the frequency of the optical field, $k = \frac{2\pi}{\lambda}$ is the wavenumber and $\phi(x, y, t)$ is the phase of the beam. For this discussion, we shall consider beams with fixed phase in time, hence $\phi(x, y, t) = \phi(x, y)$. Furthermore, for monochromatic time-harmonic electric fields, we can ignore the periodic time dependence[1] and use a more mathematically convenient notation of a complex scalar field

$$U(\boldsymbol{r}) = A(x, y)e^{j(\phi(x,y)-kz)} \tag{2.2}$$

where $U(\boldsymbol{r})$ is called the electric field phasor. Usually, we deal with the electric field in the transverse plane of propagation, thus it can be written as $U(x, y)$ at a constant value of z. Wave propagation originates from the Huygen-Fresnel principle, which states that each point of the illuminated input aperture acts as a secondary source of spherical wavelets, which can be summed to compute the electric field at a subsequent image plane. The Huygens-Fresnel integral is not ideal for computational purposes hence it is common to make the *near field* approximation which leads to the Fresnal Diffraction integral [25].

$$U'(x, y) = \frac{e^{jkz}}{j\lambda z} e^{j\frac{k}{2z}(x^2+y^2)} \iint\limits_{-\infty}^{\infty} \left[U(\xi, \eta)e^{j\frac{k}{2z}(\xi^2+\eta^2)}\right] e^{-j\frac{2\pi}{\lambda z}(x\xi+y\eta)} \mathrm{d}\xi \mathrm{d}\eta \tag{2.3}$$

which can be easily identified (apart from the multiplicative factors) as the 2D Fourier Transform ($\mathcal{F}.\mathcal{T}.$) of the expression in the square brackets with the frequency variables $f_x = \frac{x}{\lambda z}$ and $f_y = \frac{y}{\lambda z}$. (ξ, η) are the coordinates of the

---

[1] The time dependence, $e^{j2\pi vt}$, is implicit.

initial plane (located at $z = 0$) while (x, y) are the coordinates of the final plane located at a distance z. Hence, by multiplying the field by a quadratic phase factor, and then Fourier Transforming it, we can compute the field at any subsequent plane. It is most useful to view the the wave propagation phenomenon using the *systems* approach whereby we express Equation (2.3) as a convolution instead of a 2D Fourier Transform. After rearranging the terms inside the integrals, we arrive at the following equation

$$U'(x, y) = \iint\limits_{-\infty}^{\infty} U(\xi, \eta) h(x - \xi, y - \eta) \mathrm{d}\xi \mathrm{d}\eta \tag{2.4}$$

where the convolution kernel is

$$h(x, y) = \frac{e^{jkz}}{j\lambda z} e^{\frac{jk}{2z}(x^2+y^2)}$$

A single thin lens can be thought of as a spatially dependent phase transformation since light passing through it experiences variable phase delay. The effect of the lens, therefore, is to introduce a time delay proportional to the thickness of the glass at the coordinates (ξ, η). The phase profile of a thin lens is dervied in many standard textbooks on fourier optics and under the paraxial approximation, it takes the form of a quadratic function

$$\phi_f(\xi, \eta) = e^{-j\frac{k}{2f}(\xi^2+\eta^2)} \tag{2.5}$$

where f is the focal length of the lens and can be positive or negative depending on the type of lens. Using the equations above we can understand

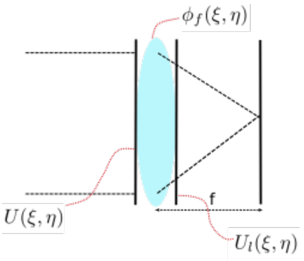

Figure 2.1: Shows how the optical fields are related at the input and the output plane of the lens. The field at the back focal plane of the lens can be computed using Equation (2.3).

how a beam of light will interact with a thin lens. If we know the electric field at the input plane of the lens, $U(\xi,\eta)$, then the electric field behind the lens, $U_l(\xi,\eta)$, will be given by the product of the lens phase profile with the input field

$$U_l(\xi,\eta) = U(\xi,\eta)\phi_f(\xi,\eta) \tag{2.6}$$

and by using Equation (2.3), we can find the electric field at any plane after the lens. For example, at the back focal plane of the lens, Equation (2.3) simplifies to

$$U'(x,y) = \frac{e^{jkf}}{j\lambda f} e^{j\frac{k}{2f}(x^2+y^2)} \iint\limits_{-\infty}^{\infty} U(\xi,\eta) e^{-j\frac{2\pi}{\lambda f}(x\xi+y\eta)} \mathrm{d}\xi \mathrm{d}\eta \tag{2.7}$$

where the quadratic phase factor of the lens cancels out with the quadratic phase factor inside the integral. Notice that in Equation (2.7), **the integral** represents an exact Fourier Transform of the incoming optical field falling at the input plane of the lens. Thus, computing the field at the focal plane becomes fast and easy. Additionally, notice that the integral above resembles the Fraunhofer approximation [25] thus a single lens takes the Fraunhofer plane (at ∞) and places it at its own focal plane (with a different scaling factor). As mentioned before, the output spatial coordinates at the focal plane are proportional to frequency variables of the Fourier Transform, $f_x = \frac{x}{\lambda f}$, $f_y = \frac{y}{\lambda f}$. The intensity, which is usually of experimental interest, is given by the absolute value squared of the electric field which means that any phase factors can be conveniently ignored.

$$I'(x,y) = \frac{1}{\lambda^2 f^2} \left| \iint\limits_{-\infty}^{\infty} U(\xi,\eta) e^{-j\frac{2\pi}{\lambda f}(x\xi + y\eta)} \mathrm{d}\xi \mathrm{d}\eta \right|^2 \tag{2.8}$$

For an optical system which respects cylinderical symmetry, we may reduce the computational complexity by using cylinderical coordinates (ρ, ϕ) and recognizing that the optical field can be written as $U(\rho)$, where ρ is the radial coordinate. [26]

2.2 Spatial Light Modulation Technology

A beam of light can be either modulated *temporally*, whereby the frequency, $v(t)$, or phase, $\phi(t)$, of a light beam is modified as a function of time, or *spatially*, which involves the time-independent manipulation of the amplitude, $A(x,y)$, or phase, $\phi(x,y)$, in the transverse plane of the propagating beam. Therefore there are two ways to spatially modulate a beam of light: i) amplitude modulation or ii) phase modulation. Examples of optical components which have been commonly used to spatially modulate a beam of light are: diffractive optical elements (DOE), holographic plates, fixed amplitude and phase masks, microlens arrays etc. These are all common optical tools to spatially modulate the beam and have been used for various applications such as to implement quantum shift registers [27], optical tweezer arrays [28] and 2p-Calcium fluorescence imaging [29], to name a few, but they do not allow full dynamic control of the imaging plane. We seek the ability to create arbitrary intensity profiles corresponding to unique optical dipole potentials which can be dynamically controlled in-situ. Two electronically controllable devices which can be useful to achieve this are: i) Phase-only SLM and ii) Amplitude SLM, both of which can be programmed using the concepts of diffraction theory as described in Section 2.1.

The Digital Micro-mirror Device is an example of a binary amplitude SLM which is used to control $A(x, y)$ in a particular plane perpendicular to the propagation direction. It has been successfully used by multiple research groups recently [30–34] to trap ultracold atoms in arbitrary trapping potentials as well as to selectively manipulate their quantum states. A typical DMD consists of ($\sim$ 1 million) tiny mirrors, each of which can be independently turned ON or OFF using an electro-mechanical torsion hinge. Despite of having an underlying mechanical structure, the DMD is surprisingly fast ($\sim$ kHz) which is a major advantage of using a DMD for trapping neutral atoms to implement fast gated-operations in quantum computing [31].

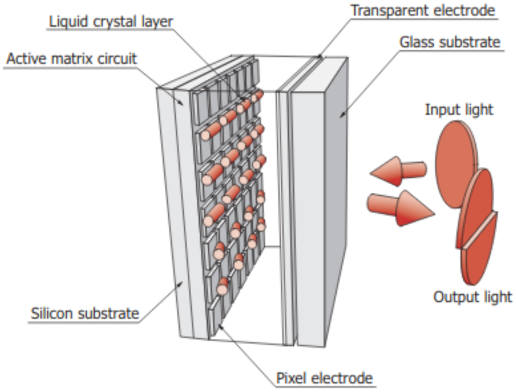

Figure 2.2: Structure of a single pixel of a phase-only SLM. The liquid crystal molecules are places in a cell squished between two electrodes. An electric field is applied across the liquid crystal layer that causes them to rotate thus changing the refractive index in the *extraordinary* direction w.r.t the *ordinary direction*. The electric field can be controlled pixel by pixel thus a spatially varying change in Optical Path Difference (OPD) is observed which manifests itself as a spatially varying phase $\phi(x, y)$. [35]

Additionally, it can show truly static images, without any flicker, certainly one less thing to worry about. For example, the DMD has been used to address single atoms in an optical lattice [36], where different lattice sites were simultaneously addressed by inducing arbitrary light shifts in a 1D chain of atoms. It is important to note that the DMD modulates the amplitude on a pixel-by-pixel basis thus beam shaping of an incoming beam can be achieved by turning certain pixels OFF while keeping others ON; this spatial multiplexing of the light field can be used to create arbitrary beam profiles by Fourier transforming the light field, using a lens for example. This process inherently causes poor light utilization since optical power is wasted by the mirrors in the OFF state. In addition, since the DMD is a binary device, there are limitations on the ability of the device for beam shaping and complex beam profiles can't be achieved [37, 38]. Futhermore, despite the fact that the DMD has been recently used to correct for aberrations [39], complete wavefront correction can not be achieved and additionally the process is based on implementing a non-binary amplitude modulation profile which requires spatially averaging a certain number of pixels thus reducing the effective resolution of the DMD. All of these reasons were convincing enough for us to not use the DMD for spatial light modulation and instead we decided to use the phase-only SLM. For a more detailed analysis on the various use cases where the DMD might be a more suitable device for modulating the input beam, the reader is referred to [40].

A phase-only SLM, on the other hand, does not affect the amplitude of the light field thus no loss of power exists[2] which allows it to achieve much higher light utilization efficiency, up to 97% [41]. In addition, the phase SLM is not a binary device, ie, it can apply 256 levels of phase modulation at each pixel, between $[0, 2\pi)$, allowing us to spatially change the phase of the light beam in the transverse plane. This provides the atomic physicist with immense control to create complex phase profiles which can correspond to some truly remarkable beam shapes [42]. Perhaps the biggest advantage of the phase-SLM is its ability to effectively and reliably correct for aberrations in the system. This is important because the vacuum viewport, in

---

[2] Except for the losses due to diffraction which would be present in both devices.

typical ultracold chambers, has been sealed tight using a metal flange which exerts stress on the edges of the silica viewport causing it to distort the wavefront non-uniformly across its aperture. This distortion of the wavefront introduces non-trivial aberrations which eventually reduce the effective resolution of the imaging and trapping system as we shall explore in the next chapter. This can be easily countered by using a wavefront sensor to measure the aberrated wavefront and then applying the inverse phase profile onto the SLM display to cancel the effect of the external aberrations. This technique has been used successfully to drastically improve the fidelity of the trapping potentials to make extremely precise ODT shapes [43]. This was successfully demonstrated by Browaeys's group (Figure 2.16) where they use a Shack-Hartmann wavefront sensor in a closed-loop configuration to feedback the instantaenous wavefront back to the SLM to correct for aberrations introduced by the vacuum viewport and any residual phase errors due to misalignments of the optical elements in the beam path. In particular, they showed that the wavefront error is mostly contributed by the vacuum viewport which was expected.

Equation (2.2) satisfies the scalar wave equation and thus serves as an appropriate description of a light field since the frequency of a monochromatic beam is usually known a priori. The SLM gives us the ability to control $\phi(x, y)$, in a plane perpendicular to the propagation direction, with a spatial resolution equal to the pixel pitch. In the next section I will combine this fact with the Fresnel Diffraction integrals to create various standard 1D and

2D trapping configurations.

We use the Hamamatsu X13138-04, a reflective type liquid-crystal-on-silicon SLM which is electrically addressed and can modulate the wavefront of an incoming light beam. As mentioned before, this SLM is a pixelated device consisting of 1280 x 1024 pixels with a pixel pitch of 12.5 μm and a maximum spatial resolution[3] 40 lp/mm. It has a rise time of 10 ms and a fall time of 25 ms and has a 96% fill factor [41].

2.3 1D and 2D trapping configurations

As was discussed in the previous sections, an SLM can apply a phase profile onto the incoming electric field, such that the resulting complex amplitude of the beam right after the SLM plane becomes

$$U(\xi,\eta) \;=\; A(\xi,\eta)e^{j(\phi+\phi_{SLM})} \tag{2.9}$$

where $\phi(\xi,\eta)$ is the original phase of the incoming beam and $\phi_{SLM}(\xi,\eta)$ is the phase imprinted by the SLM. In general, the electric field of the incoming beam is known. In our case, we select a collimated flat top gaussian beam such that the amplitude and phase profiles are (approximately) flat. Hence, we can approximate our input beam as an ideal plane wave. We developed a custom beam propagation tool in MATLAB [Appendix A], based on *Fourier Diffraction Theory*, to compute the electic field at an arbitrary plane after it

---

[3] Spatial resolution is defined in the next chapter.

passes through a set of standard optical components (lenses, gratings, prisms, cylinderical lenses etc.) separated by arbitrary distances. The intensity, which is what we measure experimentally, can be obtained by the absolute value squared of the field but it is still important to compute the electric field at every plane to find the field at any subsequent plane by the repeated application of Equation (2.3). For a single propagation, when the phase profile to be applied on the SLM is known a-priori, we can compute the intensity profile in the imaging plane of a high resolution objective by simply using Equation (2.8) with $U(\xi, \eta)$ given by Equation (2.9), with f being replaced by the $f_{objective}$. In what follows, I will use the concepts discussed above to show how we can build various standard arrangements of ODTs and control each trap depth individually by varying the power in a single microtrap, all based on diffraction theory. Furthermore, note that the $\mathcal{F}.\mathcal{T}.$ is a linear operator hence the phase profiles can be added (modulo 2π) to combine the effect of various phase profiles, for example, to translate a single ODT in 3D space.

2.3.1 3D motion of an ODT

We create a single ODT by focusing a beam of light using a single spherical singlet lens element as shown in Figure 2.3. By changing the wavefront of the incoming beam, we can precisely move this trap around in 3D space since the SLM gives us the ability to move the focus of a lens both, axially and laterally.

To move the trap axially along the longitudinal axis, we apply a quadratic phase profile corresponding to a Fresnel lens, of focal length f. This is equivalent to adding an extra lens between the beam-splitter (BS) and the *Fourier Lens*, $f_{fourier}$, in Figure 2.3 thus introducing an extra quadratic phase in the beam which will cause it to focus at a different plane as compared to the focal plane of *Fourier Lens*. The axial direction of the shift can be selected by using a positive or a negative Fresnel lens. This is important to correct for the chromatic aberration present in our custom designed objective lens. In particular, we shifted the focal plane by roughly $1\,mm$ which corresponds to the primary axial colour (PAC)[4] w.r.t the imaging wavelength of $\lambda = 461\,nm$. Similarly, to move the trap in the transverse plane, we can apply a linearly increasing phase profile which is equivalent of passing the beam through a small angle glass prism placed between the BS and the Fourier Lens. The amount and direction of the lateral shift can be controlled by tuning the magnitude and sign of the gradient of the ramp, respectively. Figure 2.4 shows the experimental as well as simulation results.

For mathematical concreteness, the phase profiles we used are given below

$$\begin{aligned} \phi_{prism}(\xi,\eta) &= \frac{k}{f_{fourier}}(\Delta x\,\xi + \Delta y\,\eta) \\ \phi_{lens}(\xi,\eta) &= -\frac{k}{2f_*}(\xi^2+\eta^2) \end{aligned} \tag{2.10}$$

where $k = \frac{2\pi}{\lambda}$, the wave vector of the light and $\frac{1}{f_*} = \frac{1}{f_{fourier}-\Delta f} - \frac{1}{f_{fourier}}$. This

---

[4] The primary axial color is a type of chromatic aberration and is outlined in the next chapter.

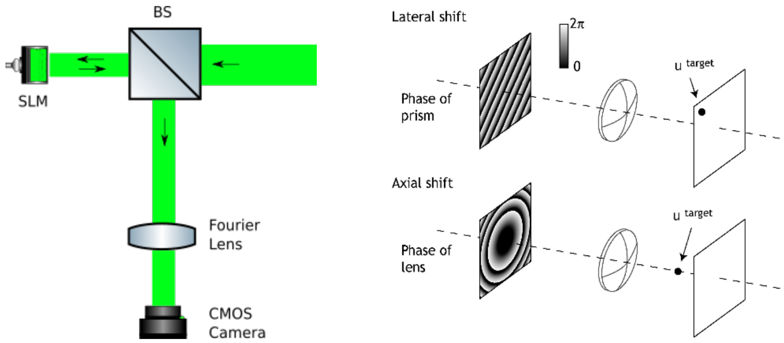

(a) (b)

Figure 2.3: (a) The optical schematic to observe the far-field diffraction pattern. The Fourier lens could equally well be a high resolution objective lens. The BS configuration employed, ensures easier alignment of the optics as compared to the small angle reflection convention. (b) The phase profiles applied onto the SLM to achieve lateral and axial shifts. The phase profiles are shown modulo(2π). The tests were performed using a collimated and expanded beam of $\lambda = 532\,nm$.

will shift the focal plane backward by an amount Δf which is what we desire since $\lambda = 461\,nm$ will focus closer to the lens as compared to $\lambda = 532\,nm$ because of the well known normal dispersion relation of decreasing refractive index with λ.

The phase profiles shown in 1D and 2D are both modulo 2π since $[0, 2\pi)$ is the unique phase range and all other values are circularly wrapped onto this range. Therefore the SLM only displays phase values within this range.[5]

Using a Fresnel lens profile, one can cause the spot to shift by a precise amount along the propagation axis of the beam. The microscope objec-

---

[5] The actual range of phase that our SLM can apply varies with wavelength. For our SLM, for $\lambda = 532\,nm$, the range of phase values $[0, 2\pi)$ is linearly mapped onto $[0, 211)$. All phase profiles generated in MATLAB were scaled accordingly.

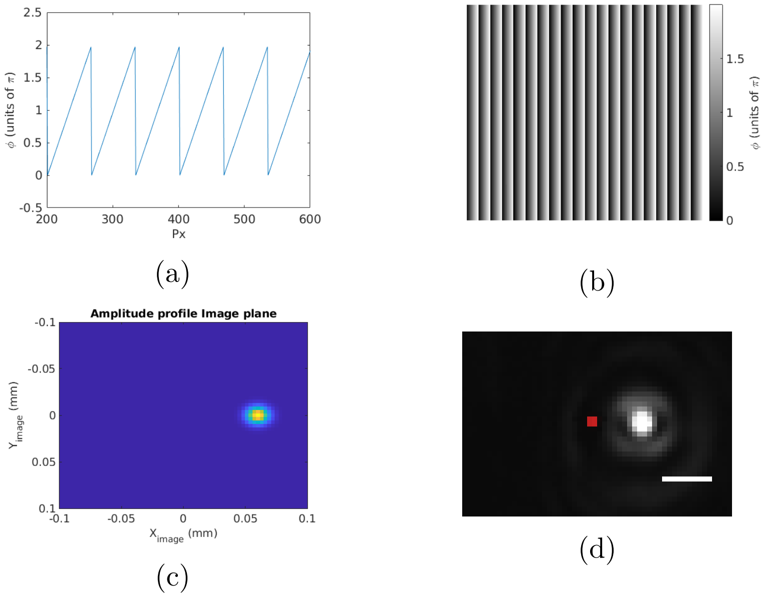

(a)

(b)

(c)

(d)

Figure 2.4: (a) A section of the phase profile of a prism in 1D with Δx set to $60\,\mu m$ in Equation (2.10). (b) The full phase profile extended to 2D to produce a lateral shift purely along the x axis. (c) Simulation results using beam propagation integrals in MATLAB. (d) Experimentally obtained image of a single focused gaussian spot. The red spot marks the location of the focus when no phase pattern is applied onto the SLM. The scale bar shown is $55\,\mu m$.

tive I designed suffers from chromatic aberration such that the focal plane at $\lambda = 532\,nm$ is displaced by $0.96\,mm$ as compared to the focal plane at $\lambda = 461\,nm$. It is important to create the ODTs in the same transverse plane as the imaging plane for optimal imaging resolution. The phase profile generated and displayed on the SLM as a correction is displayed in Figure 2.5 where I have used the $f_{fourier} = 75.08\,mm$, see Equation (2.10), corresponding to the *effective focal length* (EFL) of the objective at $\lambda = 532\,nm$.

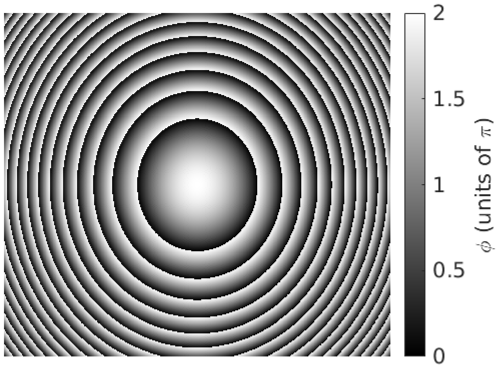

Figure 2.5: Fresnel Lens profile corresponding to a 0.965 mm shift in the focal plane to correct for the chromatic aberration in the microscope objective lens.

2.3.2 Linear Array of Optical Tweezers

The SLM can also be used to create multiple ODTs in 1D and 2D configurations using the concept of a grating phase profile. There are various types of grating profiles that one can apply and in this section we'll be exploring a few that have been commonly used in the literature. Starting with a simple 2D sinusoidal phase grating profile along the ξ axis, the complex amplitude transmittance function is given by

$$t_{grating}(\xi, \eta) = e^{j\frac{c}{2}\sin(2\pi f_0 \xi)} rect\left(\frac{\xi}{2w_x}\right) rect\left(\frac{\eta}{2w_y}\right) \tag{2.11}$$

where c represents the contrast of the phase grating, f_0 gives the frequency of the grating and w_x, w_y correspond to the width of the active area on the SLM. The $rect(x)$ function is of unit width and sets the aperture of the beam along both ξ and η axes. In specific, for our SLM, $w_x = 16\,mm$ and

$w_y = 12.8\,mm$.

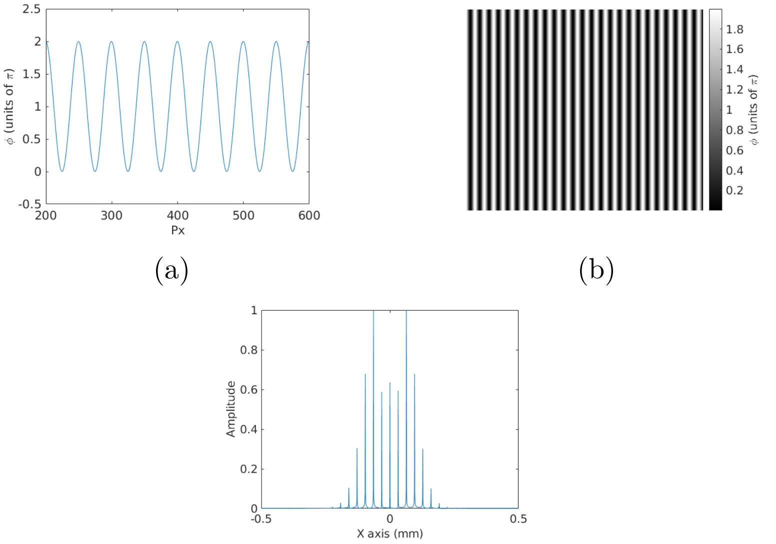

(a) (b)

(c)

Figure 2.6: (a) A section of the phase profile of a sinusoidal grating in 1D with c set to 2π in Equation (2.11). The spatial period is set to 50 px. (b) The full phase profile extended to 2D which will produce a linear array of ODTs. (c) Simulation results using beam propagation integrals in MATLAB. The computation is done in 1D for illustrative purposes with $T_s = 25\,\mu m$ and $f_{fourier} = 75\,mm$.

Using the convolution theorem

$$\mathcal{F}.\mathcal{T}.\{A(x,y)\cdot B(x,y)\} = \mathcal{F}.\mathcal{T}.\{A(x,y)\} * \mathcal{F}.\mathcal{T}.\{B(x,y)\} \tag{2.12}$$

we obtain the analytical expression of the complex amplitude profile in the fourier plane as

$$\begin{aligned}U'(x,y) = \mathcal{F}.\mathcal{T}.\{t_{grating}\} = \frac{1}{j\lambda z}e^{jkz}e^{j\frac{k}{2z}(x^2+y^2)} \\ \sum_{q=-\infty}^{\infty} J_q\left(\frac{c}{2}\right) sinc\left(\frac{2w_x}{\lambda z}(x-qf_0\lambda z)\right) sinc\left(\frac{2w_y y}{\lambda z}\right)\end{aligned} \tag{2.13}$$

The $sinc(.)$ functions are a result of the aperture of the SLM and thus their widths depend on the size of the beam passing through the fourier lens and hence the aperture of the SLM. It is straightforward to see that due to the $\mathcal{F}.\mathcal{T}.$ relation between the object and the image space, using a larger sized beam would enable us to shrink the width of the $sinc(.)$ function thus creating tighter foci. The Bessel function of the first kind, $J_q(.)$ is the envelope of the diffraction pattern and sets the peak intensity of various orders while the train of pulses is produced by the sinusoidal nature of the phase grating. The results are plotted in Figure 2.6. If we keep $wf_0 \gg 1$, then there is negligible overlap of the various diffraction orders as shown in Figure 2.6c, thus the $|U'|^2$ can be approximated as the squared sum of the individual terms dropping all cross-terms

$$I'(x,y) = \left(\frac{1}{\lambda z}\right)^2 \sum_{q=-\infty}^{\infty} J_q^2\left(\frac{c}{2}\right) sinc^2\left(\frac{2w_x}{\lambda z}(x-qf_0\lambda z)\right) sinc^2\left(\frac{2w_y y}{\lambda z}\right) \tag{2.14}$$

To vary the power in the different diffraction orders (which equivalently translates to varying the trap depths), we use the fact that for a sinusoidal grating, the peak amplitude of a particular order is proportional to $\left(\frac{J_q(c/2)}{\lambda z}\right)^2$. Thus, by varying the contrast we can control the relative power in the various orders. In addition, notice that distance between two orders is $f_0 \lambda z$ is directly proportional to the frequency of the grating. Figure 2.7 shows the effect of varying the contrast and frequency of the phase grating on the peak intensity and relative peak location, respectively.

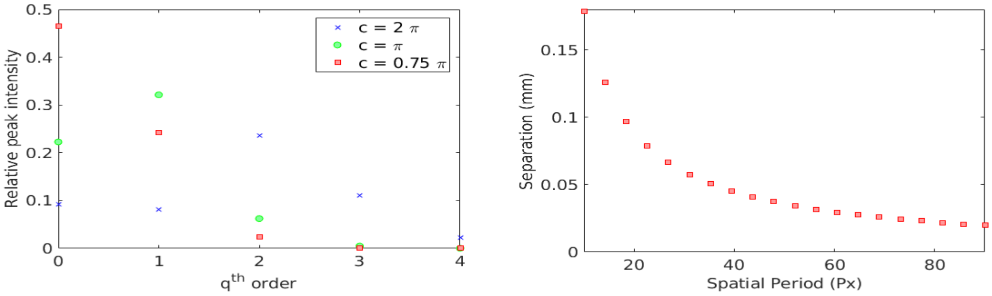

(a) (b)

Figure 2.7: (a) Shows the variation of the relative power in various orders as the contrast of the phase grating is varied. (b) Shows the separation between two ODTs can be varied by tuning the frequency of the phase grating. Here $f_{fourier} = 42\,mm$.

In addition to the sinusoidal phase grating, we can also use a square grating profile. The mathematical analysis for an analytical solution follows closely to that of the sinusoidal grating with the exception that the envelope function is also a $sinc(.)$. Again there are two parameters associated with this phase grating: i) contrast ii) spatial period. We generate binary phase grating profiles of two different spatial periods and add them (modulo 2π).

$$\begin{aligned} U_1(\xi,\eta) &= |U_1| e^{j\phi_1} \;\; (field\, 1) \\ U_2(\xi,\eta) &= |U_2| e^{j\phi_2} \;\; (field\, 2) \\ U_{total}(\xi,\eta) = U_1(\xi,\eta)\, U_2(\xi,\eta) &= |U_1||U_2| e^{j(\phi_1+\phi_2)} \end{aligned} \tag{2.15}$$

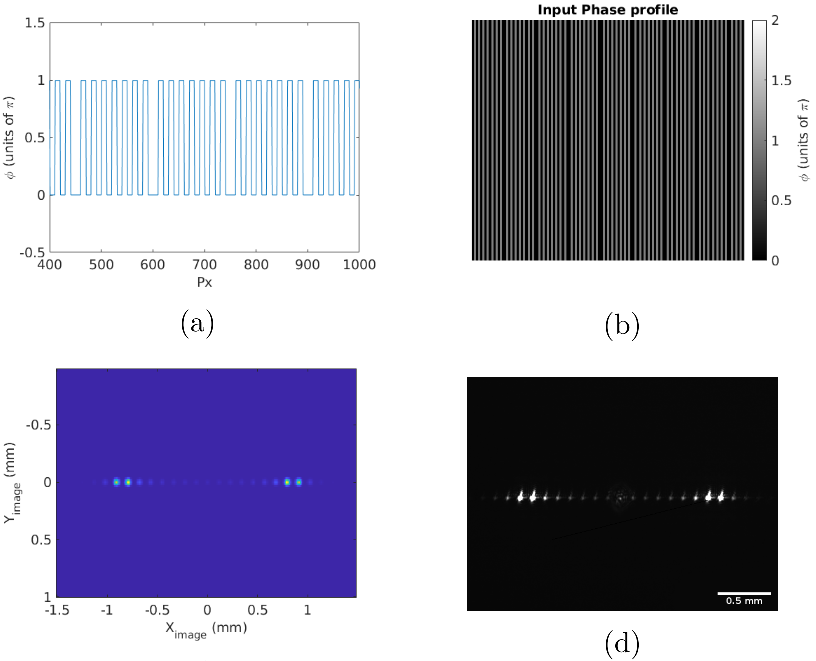

(a) (b)

(c) (d)

Figure 2.8: (a) A small section of the phase profile of a binary phase grating in 1D with $c = \pi$. By choosing this value of the contrast, the 0^{th} order is diminished. Note that the phase profiles were added modulo 2π. (b) The same phase profile extended to 2D to produce an array of traps inside each order. (c) Simulation results using beam propagation integrals in MATLAB. Notice that the 0^{th} order is diminished. (d) Experimentally obtained image of an array of traps. The experimental results of the location, size and trap separation agree well with the simulations.

This addition of a high frequency grating and a low frequency grating is produced by multiplying the corresponding optical fields which corresponds to the convolution of their resulting fourier transforms using Equation (2.12). This technique is used to get rid of the 0^{th} order, which is sometimes undesirable since it remains unaffected by any phase modulation applied on the SLM. By adding another low frequency grating profile on top of an existing high frequency grating, we can modulate within each order as a consequence of the convolution theorem. This is particularly useful for us experimentally since we always select the 1^{st} order using a fixed pinhole (Figure 2.9) and create the traps by modulating within that order. Figure 2.8 shows another beam propagation simulation and its corresponding experimental result showing the creation of a 1D array of traps within each order. As described in the next chapter, we shall only use the 1^{st} order to create our ODTs. Whether we use a binary grating or a sinusoidal grating, both suffer from a mathematically inherent problem of a decreasing envelope. In particular, for a sinusoidal phase profile, the envelope is a bessel function of the 1^{st} kind while for a binary grating profile, the envelope is that of a $sinc(.)$ function. Figure 2.8d shows the experimentally obtained intensity profile in the fourier plane of a 400 mm lens where the intensity is seen to decrease as we move away from the center of a particular diffraction order. This problem can be avoided by specially designing binary phase gratings which are optimized to keep the intenisty uniform across a pre-defined set of spots. In the next section, a binary Dammann phase grating profile is designed to create equal intensity focused spots in the fourier plane of a lens. Considerable work has been done on the design of Dammann phase profiles and the interested reader is referred to [44–49].

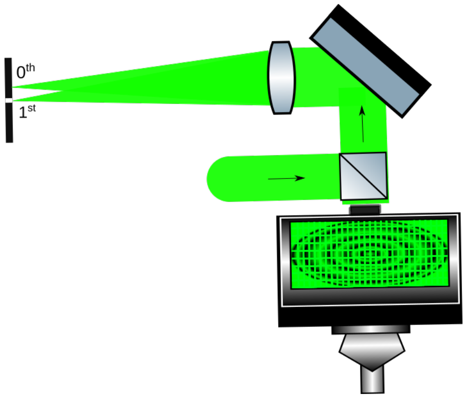

Figure 2.9: We use an intermediate focal plane to spatially filter out all orders except the 1st. The 1st order contains all the information and at the same time has the highest power.

2.3.3 Optimizing the trap depths

We have seen in the section above how to split a single beam into an array of spots in the fourier plane of a lens. This process has been of considerable interest for switching systems, in the past, to supply optical power to arrays of components such as digital-optical logic gates, optically bistable devices or electro-optical modulators. All of these applications require uniform intenisties across all spots. A lot of work has been done on improving Dammann gratings to ensure precisely uniform illumination across the focused spots in a 2D array. We use a binary Dammann phase profile to ensure a uniform trap depth (within 2%) across a 1D and 2D array of ODTs. The design process involves optimization, therefore we start by defining a merit function[6] which is selected as the standard deviation of the peak intensities of N spots in the array, where N is the number of ODTs to be created. As we shall soon see, there would be multiple diffraction orders (beyond N), but for experimental purposes, they shall all be ignored since their peak intensities will not be uniform with the N traps of interest.

In the previous section we generated a phase profile by summing *two* square waves of different frequencies. A typical binary Dammann grating can be viewed as a weighted sum of *multiple* square waves of varying frequencies such that the resulting fourier transform of the modified electric field generates the desired number of traps with the appropriate spacing. It has been shown in [48] that as the size of the desired array grows, the degrees of freedom increase thus causing the computational complexity to rise exponentially. We choose an arbitrary contrast level of π, thus the degrees of freedom (d.o.f) in the optimization process are merely the transition points in a single period (see Figure 8).

Let the size of the array be $N = 2M + 1$ where M labels the diffraction order corresponding to a single trap[7]. Since a binary phase grating produces equal intensities in the positive and negative orders (symmetric about the 0^{th} order), thus we require approximately $\frac{N}{2}$ d.o.f [49, 50]. By varying these set of unknown transition points for a normalized single period of the grating, we minimize the merit function to within 2% intensity variation. Figure 2.11

---

[6] Also called an objective function or cost function.

[7] The orders go from $-M^{th}$ to $+M^{th}$ including the 0^{th} order.

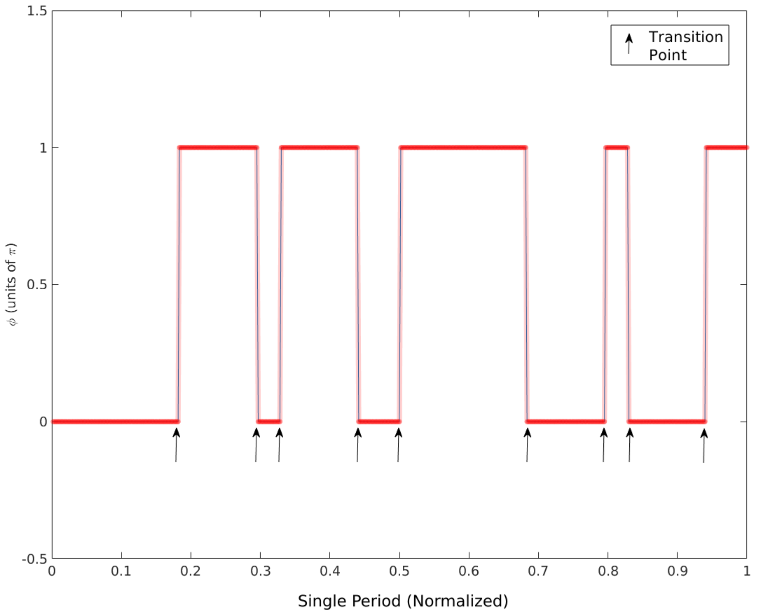

Figure 2.10: A single period of an optimized Dammann phase grating to generate a linear array of 8 ODTs of equal peak intensities. The transition points used for optimization are marked with the arrows. Notice that the transition points are symmetric in the sense that starting from 0.5, the values at which the transitions occur are exactly the same as the first 4 transition points starting from 0. Thus, the d.o.f for this optimization routine were chosen to be $\frac{N}{2} = 4$.

shows the simulation and experimental results obtained where we closely followed the procedure by Walker and Morrison [48, 49] for an array of size $N = 8$ and $N = 13$.

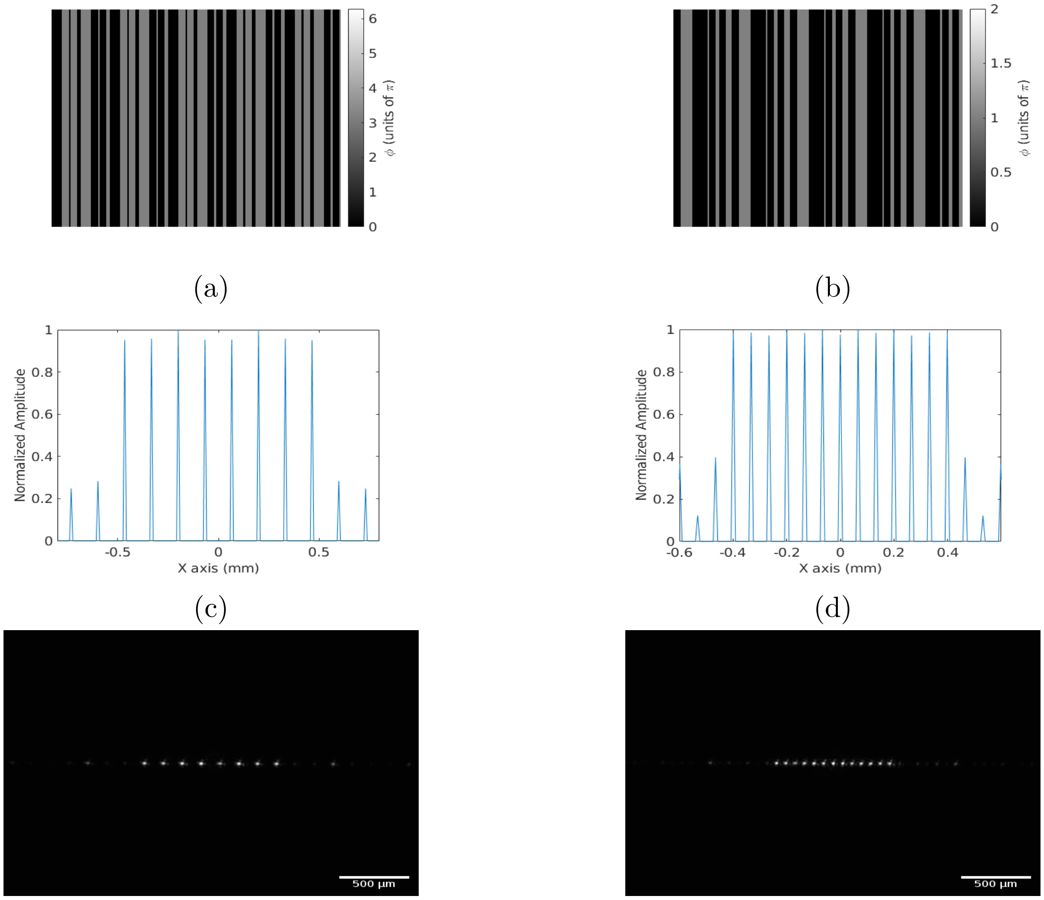

(a) (b)

(c) (d)

(e) (f)

Figure 2.11: The optimized phase profile for a Dammann grating to produce a 1D array of (a) 8 and (b) 13 ODTs. (c),(d) 1D Simulation results using beam propagation integrals in MATLAB. Notice that the 0^{th} order is diminished for an even number of traps. The simulations were performed by choosing the $f_{fourier} = 400\,mm$ and $T_s = 12.5\,\mu m$. (e),(f) Experimental results of 1D arrays, imaged in the fourier plane of a $400\,mm$ lens, by displaying the phase profiles along with the appropriate wavefront correction (Figure 2.13) onto the SLM. Notice that the experimental results again agree precisely with the simulation results and the location of the spots are exactly as predicted by the beam propagation code.

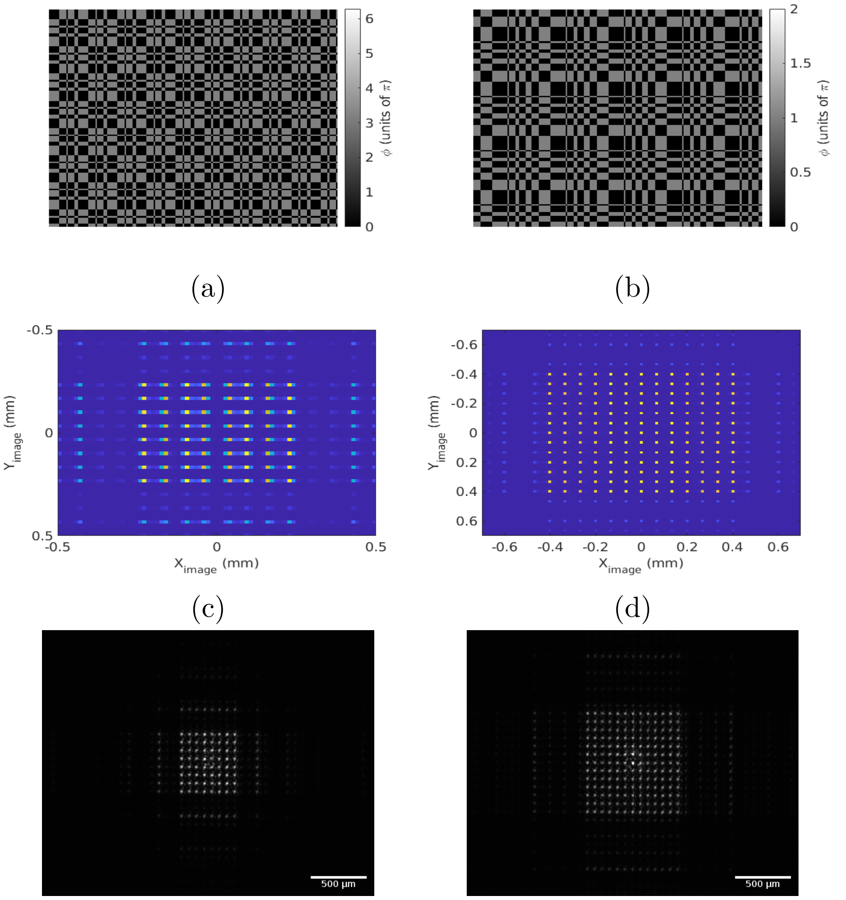

(a) (b)

(c) (d)

(e) (f)

Figure 2.12: The optimized phase profile for a Dammann grating to produce a 2D array of (a) 64 and (b) 169 ODTs. (c),(d) 2D Simulation results using beam propagation integrals in MATLAB. Notice that the 0^{th} order is diminished for an even number of traps. The simulations were performed by choosing the $f_{fourier} = 400\,mm$ and $T_s = 12.5\,\mu m$. (e),(f) Experimental results of producing 2D arrays of 64 and 169 ODTs, respectively, by displaying the phase profiles along with the appropriate wavefront correction provided by the manufacturer (Figure 2.13). Notice again that the experimental results agree with the simulation results obtained from the beam propagation code.

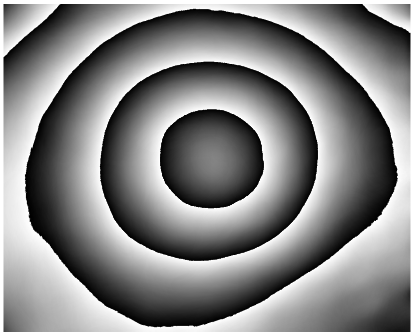

Figure 2.13: The wavefront correction, provided by Hamamatsu, which must be applied to any computer generated hologram (CGH) before uploading onto the SLM. This corrects for the non-linearities in the response of the pixels due to manufacturing defects in LCD display of the SLM.

2.4 Arbitrary Trapping Geometries

Up until now we have only considered standard ODT geometries such as 1D and 2D gratings. For arbitrary beam shaping, there are various computational imaging algorithms available which iteratively compute the phase profile required to produce a given intensity distribution. Here we show the use of the most basic phase reconstruction algorithm known as the Gerchberg-Saxton (GS) Algorithm which has been used extensively for various applications in ultracold atomic physics such as realizing quantum Ising models using Rydberg atoms [51] and to create highly uniform micro-trap arrays [52].

We already know that the relationship between the field at the SLM plane and the image plane is that of a $\mathcal{F}.\mathcal{T}.$. The goal of the phase retrieval algorithm is to find the phase profile at the SLM plane such that, when Fourier Transformed, it would produce the target intensity distribution in the image plane. As you can probably notice, the amplitude in the SLM plane as well as the phase in the image plane are unspecified and hence unconstrained. For ultracold systems, it is well known that for a FORT under the dipole-approximation, the phase of the light doesn't affect the trapping profile. Hence the phase in the **image plane** is truly unconstrained. On the other hand, the amplitude profile in the SLM plane could in principle be anything, but for all practical purposes, it more often than not a 2D gaussian.

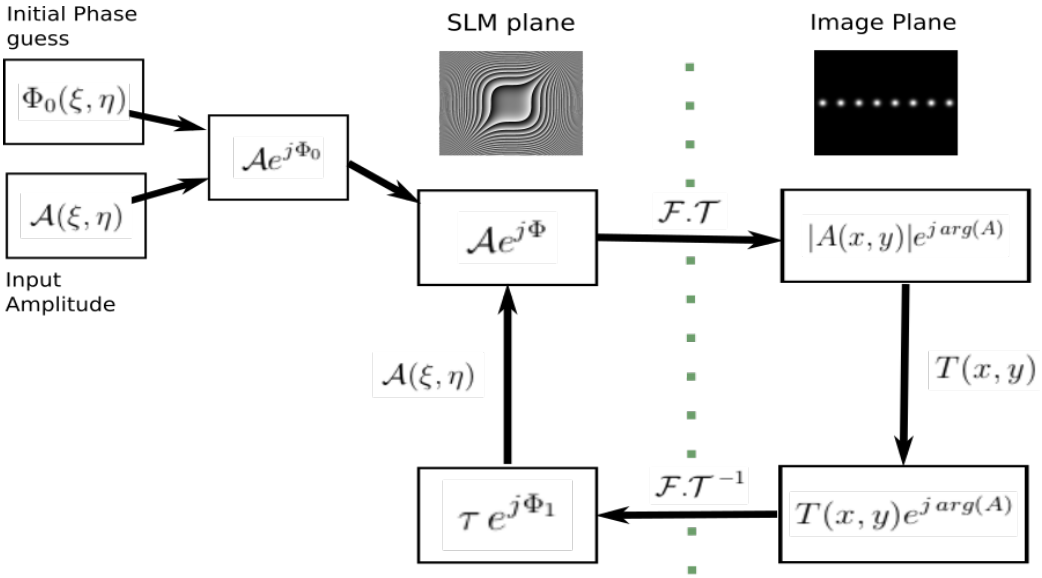

Figure 2.14: The flow chart for the GS algorithm for shaping the intensity profile of an incoming beam. At the image plane, the magnitude of the field is replaced by the target field amplitude before taking the inverse $\mathcal{F}.\mathcal{T}$.. Subsequently, at the SLM plane, the magnitude of the resulting field is replaced with the fixed amplitude profile of the input beam before moving on to the next iteration.

To illustrate the importance of understanding the constraints, let us take the naive approach (see Figure 2.15) of simply using the *inverse* $\mathcal{F}.\mathcal{T}$. of the

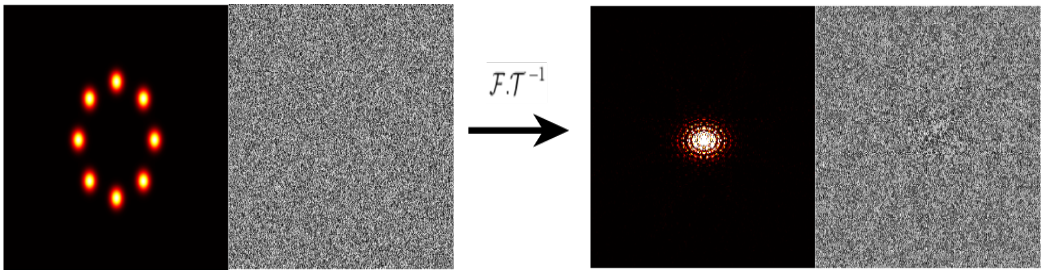

Figure 2.15: The *inverse* $\mathcal{F}.\mathcal{T}.$ of a ring lattice ampltidue distribution along with a random phase distribution. The required electric field at the SLM plane is computed in MATLAB. The required amplitude profile looks equally daunting as the phase profile and the SLM can't modulate both at the same time.

amplitude profile $U'(x,y) = \sqrt{I(x,y)}$ combined with a random phase profile. This gives us the required field at the SLM plane which includes an amplitude as well as a phase profile to modulate the incoming beam. This is clearly useless for us since we can only modulate the phase of the incoming beam but not its amplitude. Thus the amplitude profile right after the SLM would be exactly the same as at the input of the SLM, which is usually selected to be a gaussian.

The GS algorithm circumvents [53] this issue by incorporating an iterative sequence of $\mathcal{F}.\mathcal{T}.$ and *inverse* $\mathcal{F}.\mathcal{T}.$ and repeatedly constraining the system with the gaussian input amplitude profile. At each iteration, the error between the target intensity distribution and the predicted intensity distribution is computed and serves as the *merit function* of the optimization routine. The procedure of the GS algorithm is as follows:

(i) The spatial amplitude profile in the SLM plane is $\mathcal{A}(\xi, \eta)$, and remains fixed during any iteration. The initial phase $\Phi_0(\xi,\eta)$ is chosen to be a random phase profile. This sets the optical field in the SLM plane as $\mathcal{A}(\xi,\eta)e^{j\Phi_0(\xi,\eta)}$.

(ii) The optical field in the image plane of the objective is obtained by $\mathcal{F}.\mathcal{T}.[\mathcal{A}e^{j\Phi_0}] = |A(x,y)|e^{j\,arg(A(x,y))}$

(iii) $|A(x,y)|$ is then replaced by the target amplitude profile $T(x,y) = \sqrt{I(x,y)}$ to set the new optical field in the image plane as $T(x,y)e^{j\,arg(A(x,y))}$.

(iv) This field is *inverse* $\mathcal{F}.\mathcal{T}.$ to obtain the $\tau(\xi,\eta)e^{j\Phi_1(\xi,\eta)}$.

(v) $\tau(\xi,\eta)$ is subsequently replaced by the fixed input amplitude profile $\mathcal{A}(\xi,\eta)$ to set the new optical field in the SLM plane as $\mathcal{A}(\xi,\eta)e^{j\Phi_1(\xi,\eta)}$.

(vi) Steps (ii)-(v) are iterated over and over until the error between $T(x,y)$ and $A(x,y)$ drops below an arbitrary threshold.

The block diagram of the GS algorithm is shown in Figure 2.14. Note that the error function can be arbitrarily defined, and, in our case, we choose the RMS error which is given as

$$\varepsilon = \sqrt{\frac{1}{N}\sum_{x,y}(T^2(x,y) - A^2(x,y))^2} \tag{2.16}$$

where N is the total number of pixels used in the computation.

In addition, it is possible to feedback the in-situ intensity pattern and then make small corrections to the target amplitude profile $T(x,y) + \varepsilon(x,y)$

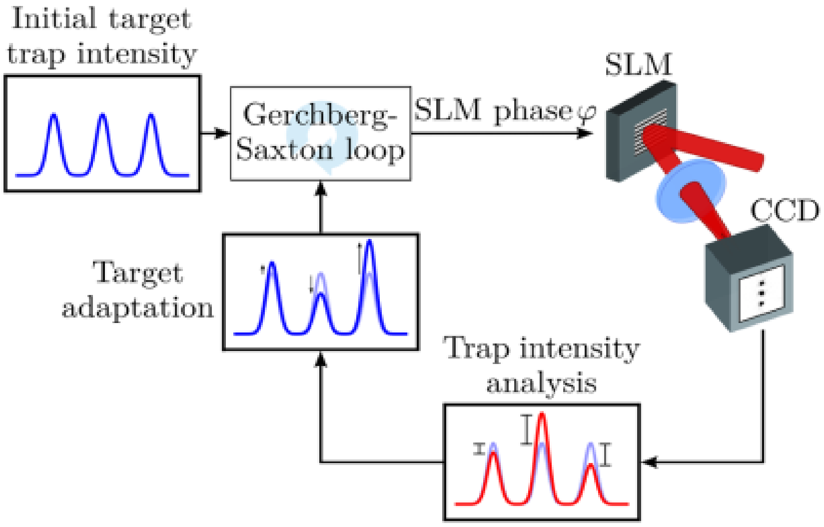

Figure 2.16: The GS algorithm may be modified by feedbacking the actual image of the traps and correcting the target intensity profile to improve the uniformity in the trap depths [43].

to obtain very high fidelity arrays of ODTs. This can be done by modifying the GS algorithm and was demonstrated in [43] to improve the uniformity of the trap depths in real-time Figure 2.16.

It is worth mentioning that using the GS algorithm alone without feedback results in *grainy* intensity profiles (ie, containing high frequency noise). This can be minimized by either using fluoroscence imaging feedback or alternative algortihms such as using conjugate gradient minimization [54]. The experimental results shown in Figure 2.17 clearly show noisy ODTs which are not ideal and would cause heating in the trap.

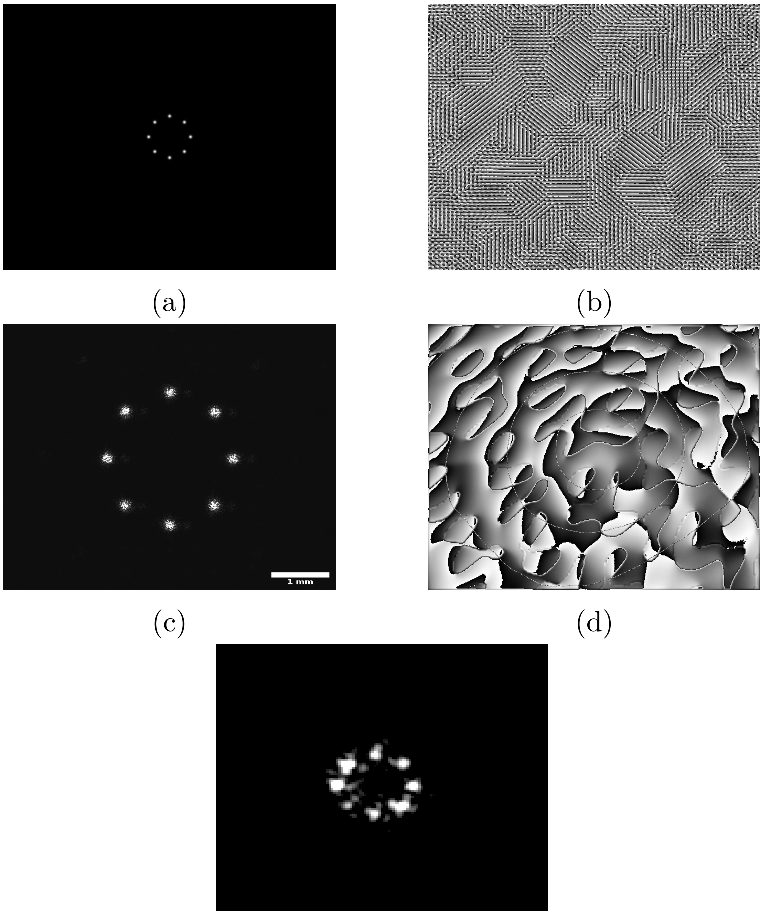

(a) (b) (c) (d) (e)

Figure 2.17: (a) Shows the target intensity profile input to the GS algorithm. (b) The phase profile generated after 50 iterations. (c) Experimentally obtained image using a $f_{fourier} = 400\,mm$ lens. The noise in the image is a result of the GS algorithm not converging to a low enough error (Equation (2.16)). The result is improved by giving the GS algorithm an improved initial guess for phase profile (d). (e) As a result, the characterstic grainy noise of the GS algorithm is removed. Although the traps are not all of equal intensity, this can easily be corrected by introducing feedback as mentioned briefly in Figure 2.16.

2.5 Heating in the SLM Trap

The toggle rate of the Hamamatsu SLM is around 800 Hz while the response time of the liquid crystal is much slower at around 50 Hz. If we look at the time-frequency spectrum of the power fluctuation in the beam after reflecting off the SLM, there is a clear peak around this toggle frequency. The magnitude of this intensity fluctuation is only $\simeq 1\%$ of the signal amplitude yet it can cause undesirable heating in the ODT if the resonance condition is met. It was shown by [55] that, if the frequency of fluctuation is twice (or a multiple of 2) that of the trap frequency, then the atomic motion can be resonantly driven inside the trap causing parametric heating. This eventually leads to loss in atom number [56]. For our setup, the trapping frequency therefore should not be close to 400 Hz, 200 Hz etc. Although the SLM has not been tested with trapped atoms, yet it is important to note that if such a situation arises, an AOM (acusto-optic modulator) should be used to flatten off the intensity fluctuation by a simple feedback loop.

Chapter 3

Optical Imaging System

With the goal to study the quantum effects at the single Rydberg atom level, high-resolution in-situ imaging of individual atoms precisely localized in extremely tight optical dipole traps (ODT) is an indispensable tool in modern ultracold experiments. This has been used, for example, to directly observe the superfluid to mott transition at the single atom level [57], for simulating the quantum Ising model [51] and for quantum computation [2, 58]. Using the technique of assembling an array of ODTs, consisting of a large number of identical Rydberg atoms, significant progress has been made towards achieving high-fidelity quantum control of Rydberg-atom qubits [59], a promising area for quantum computation. To image Rydberg atoms suspended in an ODT, a few research groups have placed the objective lens directly inside the vacuum chamber [60, 61]. This has the advantage of enjoying a very high numerical aperture (NA), however such lenses need to be specially designed to be compatible with an ultra-high vacuum environment (1x10^{-11} Torr). In addition, most commercial solutions are either outrageously expensive or use soft structural adhesives [62] that have high outgassing rates which limits the lowest acheivable pressure for Ultra High Vacuum. We trade a high NA for a longer working distance-the distance between the last optical surface and the back focal plane-so that the objective lens is placed outside the vacuum chamber.

In this chapter, I will describe the design of an infinity corrected, high-resolution, low-cost, long working distance, objective lens consisting of four[1] commercial spherical singlets from ThorLabs. Since the vacuum window introduces significant spherical aberrations, it must be taken into account during the design process, thus essentialy we are faced with a five-element, lens design problem. For our experiment, it was important for this custom objective to be diffraction-limited for dual wavelengths: the 461 nm Sr tansition which is used for flouroscence imaging and the 532 nm (Coherent Optics Verdi V-Series) light used to create far off resonant optical dipole traps (FORT) [63, 64]. The limit on the maximum acheivable optical resolution is imposed by the numerical aperture (NA) of the vacuum viewport. In our current experimental setup, the diameter of the vacuum viewport is 29 mm while the distance to the center of the chamber is 52 mm which sets the maximum achievable NA $\simeq 0.28$. The Rayleigh criterion subsequently

---

[1] Acceptable performance could not be reached with three lenses.

sets the diffraction limited resolution at $\lambda = 461\,nm$ to be

$$\frac{1.22\lambda}{2NA} = 1.01\,\mu m$$

This novel microscope objective lens features a diffraction limited resolution of $1.2\,\mu m$, a working distance of around $90\,mm$ and a field of view (FOV) spanning over $350\,\mu m$, which can be used to image more than 500 x 500 lattice sites in a typical optical lattice [65]. Table 3.1 shows some of the key features of our custom designed microscope objective lens.

	$461\,nm$	$532\,nm$
Optical Resolution	$1.16\,\mu m$	$1.36\,\mu m$
On-Axis Strehl Ratio	0.93	0.81
Working Distance	$87.96\,mm$	$88.81\,mm$
Field of View	$350\,\mu m$	$210\,\mu m$
Depth of Field	$4.0\,\mu m$	$4.7\,\mu m$
Collimated Beam Diameter	$35.6\,mm$	$36.0\,mm$
Numerical Aperture	0.240	0.237
Collection Angle	27.9°	
Collection Solid Angle	$4\pi \times 0.015$ sr	
Chromatic Shift	0.96 mm	

Table 3.1: A summary of the important parameters of the designed microscope objective.

3.1 Optical Design

3.1.1 Introduction to Optical Design

OSLO is one of the many examples of optical design software out there that can be used to design, analyse and optimize complex imaging optics as well as illumination systems. An example of an imaging system is a camera lens Figure 3.1a or an infinity-corrected microscope objective. OSLO can also be used to perform Gaussian beam analysis on an optical system, for example, to find the right lenses to optimally couple light into a single mode fiber. In addition, it can be used to find the coupling efficiencies into *multimode* and *polarization maintaining* fibers. Lastly, once the optical design is complete, it is commonly used for tolerancing analysis to study the effects of manufacturing defects as well as assembly errors. From what follows, we'll be assuming all units are in mm unless otherwise stated.

(a) A wide field camera lens.

(b) The first iteration of our custom designed objective.

There are two main regimes used for evaluating the performance of an optical system: i) the geomterical optics mode which uses ray-tracing and ii) the physical propagation of light which uses direct integration.

Ray Tracing

There are two aspects of ray-tracing which are used by all optical design computational environments: i) propagation of a ray through a medium and ii) refraction of a ray at a boundary. The former is usually more computationally expensive. Ray tracing is done by first discretizing space into blocks and then using multiple iterations, one for each discrete space block, to propagate a single idealized ray (a vanishingly narrow beam of light) from the object surface to the image surface. A perfect ray is assumed to be linear over a localized region of space. If the medium is isotropic and homogenous, rays will propagate along straight lines. As seen in Figure 3.2, the translation step involves computing the intersection of a line and a surface, while the refraction step involves applying Snells law at the point of incidence:

$$\begin{aligned} \boldsymbol{n} \times \hat{\mathbf{k}} &= \boldsymbol{n'} \times \hat{\mathbf{k}} \\ n \sin(i) &= n' \sin(i') \end{aligned} \tag{3.1}$$

Recall that a ray can be described by a vector $\boldsymbol{n}$ in the direction of propagation with a magnitude equal to the refractive index of the medium in which it propagates. Equation (3.1) says that the tangential component of the ray vector is continuous at the interface between two refracting media; a trivial result which can be directly derived from Maxwell's equations in integral form [66].

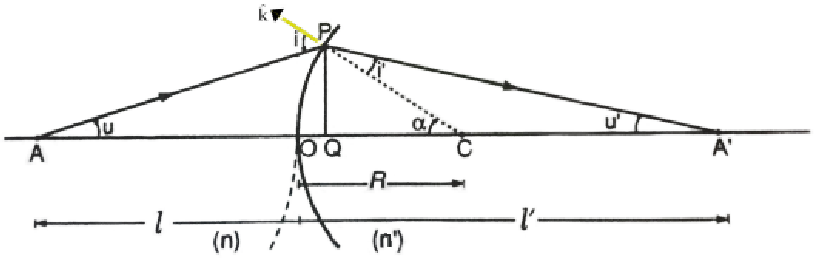

Figure 3.2: Conventions used for a ray trace diagram. Point P is the point of intersection between the ray which originates from the object point at A in the direction u and, the refraction surface of radius R centered at C. The refractive index is denoted by n while the thickness of the object is denoted by l. Primed coordinates refer to the image space while unprimed coordinates are for the object space. The radius of curvature of the surface shown is +ve, $|R|$, and $\hat{\mathbf{k}}$ is the normal to the surface at P.

Paraxial optics deals with the propagation of light through a centered optical system (not necessarily rotationally symmetric) which has the propery that a ray which is sufficiently close to the optical axis *at all points*, will have its angle of incidence on all surfaces necessarily small, hence $\sin(i)$ can be approximated by the angle itself, and the law of refraction becomes:

$$ni = n'i' \tag{3.2}$$

The ray trace equations under the paraxial approximation are given in Equation (3.3) where the first equation is the transfer equation while the second equation is the refraction equation at a particular surface. Note that it is sufficient to trace merely two rays to determine the location of the image point since all paraxial rays leaving a particular object point converge to the same image point. The paraxial approximation is commonly used by the design software to quickly determine the location of the image, the principal planes, the *effective focal length* (EFL), the NA, the image height etc.

$$\begin{aligned} h_{t+1} &= h_t + d_t u'_t \ (translation) \\ n'_t u'_t - n_t u_t &= -h_t \frac{1}{R}(n'_t - n_t) \ (refraction) \end{aligned} \tag{3.3}$$

Where h_t is the height of the ray at the t^{th} surface, while d_t is the thickness of the t^{th} surface[2]. If it's not obvious, note that $u'_t = u_{t+1}$ and $n'_t = n_{t+1}$. The sequential application of the paraxial translation and refraction equations allows one to trace any paraxial ray through an optical system. There are multiple algorithms used to implement the above set of equations in computer programs to execute successful paraxial ray tracing but these are not discussed here and the interested reader is referred to [67].

Table 3.2 shows the result of a paraxial ray trace through the custom objective in OSLO. The first column numbers the surfaces from 0 (object surface placed at ∞ in this case) to 11 (image surface representing the center of the vacuum chamber). As mentioned earlier, this is a five element design and hence the number of surfaces of the optical system are labelled 1-10. OSLO gives us the data for the height (h in mm) and slope (u in $^\circ$) of the marginal and the chief rays.

The marginal ray (also called the axial ray) is defined as the meridional ray (a ray lying in the Y-Z plane: see fig. 3.3) which starts from the center

---

[2] Thickness of the t^{th} surface is the distance between the surface $t + 1$ and surface t.

	Marginal Ray		Chief Ray	
Surface	$h(mm)$	$u(°)$	$h(mm)$	$u(°)$
0	0.0000	0.000	∞	0.076
1	17.8000	0.000	-0.0711	0.050
2	17.8000	6.879	-0.0676	0.050
3	22.2317	2.393	-0.0352	0.036
4	22.4905	0.369	-0.0312	0.060
5	22.6832	4.694	0.0000	0.039
6	22.1350	7.142	0.0046	0.060
7	22.0728	11.395	0.0051	0.038
8	21.8479	13.714	0.0092	0.059
9	13.6625	9.149	0.0449	0.040
10	12.2385	13.714	0.0467	0.059
11	0.0000	13.714	0.1000	0.059

Table 3.2: Paraxial ray trace of the marginal and chief rays through the designed objective lens at 532 nm. The input beam radius is chosen to be 17.8 mm and the object side half-field angle is chosen to be 0.077° to ensure that the height of the image is 100 μm.

of the object point at the optical axis, and touches the maximum aperture of the optical system. In this way, the marginal ray is useful in determining the aperture height of a designed lens. We can see this clearly from the table where the value of h at surface 5 is the highest among all surfaces, which implies that SRF 5 serves as the limiting aperture of this optical system. It might seem like we still have some room for the aperture height to go even higher (all the way to 25.4 mm) but remember that 0.1" from the edge is deliberately left for the thickness of the lens spacers [Appendix B]. Just for completeness, the location at which the marginal ray meets the optical axis determines the location of the image surface. Notice further that the value of u at SRF 11, gives us the image space NA by $NA = \sin(u) = 0.237$. The value of h at SRF 0 and SRF 11 is zero by definition of the marginal ray.

The chief ray is defined as a meridional ray which starts from the edge of the object and passes through the center of the aperture stop. In this way, the chief ray determines the location of the aperture stop. We can again see this clearly from Table 3.2 where the value of h at SRF 5 vanishes which means the ray being traced cuts the optical axis at SRF 5, then, by definition SRF 5 is the aperture stop of the system. The chief ray also tells us about the height of the image: the value of h at SRF 11 is 100 μm.

To evaluate system performance more accurately, in particular, compute the aberration coefficients, real ray tracing is required where Snell's law is obeyed exactly as stated in Equation (3.1). Lets look at a real ray trace, shown in Table 3.3, through our custom designed objective and compare the results with the paraxial ray trace done earlier. We shall again trace the marginal and the chief ray to make a fair comparison and demonstrate OSLO's power.

The values of the ray traces in Tables 3.2 and 3.3 look approximately the same but not quite exactly identical. Paraxial ray tracing gives us an idealized version of how the rays would travel through the system. The information about how the rays *actually* travel through the system is given by the real ray trace, which is more accurate. Hence the results obtained through the trace are used by the design software to extract information about the aberrations in the optical system. Notice that in the last row (at

	Marginal Ray		Chief Ray	
Surface	$h(mm)$	$u(°)$	$h(mm)$	$u(°)$
1	17.8000	0.000	-0.0711	0.050
2	17.8000	7.178	-0.0676	0.050
3	22.3516	2.538	-0.0352	0.036
4	22.5172	0.574	-0.0312	0.060
5	22.8589	-4.715	0.0000	0.039
6	22.5494	-7.174	0.0046	0.060
7	22.0049	-11.503	0.0051	0.038
8	21.2529	-13.791	0.0092	0.059
9	13.1027	-9.199	0.0449	0.040
10	12.6708	-13.791	0.0467	0.060
11	0.0002	-13.791	0.1000	0.060

Table 3.3: Real ray trace of the marginal and chief rays.

the image surface) of Table 3.3, the height of the marginal ray is $\simeq 0.2\,\mu m$ (small indeed since this objective has been corrected for aberrations) but not exactly 0 what we expected it to be, by definition. The reason for this discrepency is the residual on axis Spherical Aberration, which I shall delineate in the next section.

Diffraction of light

Using the direct integration approach, which is based on wave-optics, presents a more accurate description of how a light beam evolves through an optical system. This approach is based almost entirely on the scalar wave approximation. The diffraction limit of a system is only explained when we take the wave nature of light into account. OSLO uses the Fresnel Diffraction integrals to propagate the wavefront from one plane to another, the theory of which was discussed in detail in the previous chapter.

3.1.2 Why Does It Work: Performance Evaluation

To understand and calculate how a lens performs under real test conditions I will use several metrics to describe various aspects of its performace such as Modulation Transfer Function (MTF) curves, the spot diagram analysis and ray-intercept curves. To completely specify an optical design, it is convenient to use the *lens surface data* table as shown in Table 3.4. It contains the curvatures, thicknesses and the materials of all the surfaces making up the system.

Surface	Radius	Thickness	Material
1	∞	4.0	NBK-7
2	77.2	37.000	Air
3	205.0	6.2	NBK-7
4	-205.0	29.887	Air
5	90.1	6.7	NBK-7
6	∞	0.500	Air
7	65.2	6.2	NBK-7
8	171.6	34.525	Air
9	∞	2.667	Corning 7056
10	∞	50.665	Vacuum

Table 3.4: Lens Surface Data. The lenses used (SRF 2-8) are all from Thorlabs: LC1611, LB1199, LA1399 and LE1015. All units are in mm.

As mentioned before, we used 2" commercial spherical lens elements from ThorLabs, and the radii of curvatures as well as thicknesses were taken from their online list of catalog lenses. The material column shows the optical material used *after* the corresponding surface. Merely entering this lens surface data into OSLO autmatically generates the lens drawing as shown in Figure 3.3.

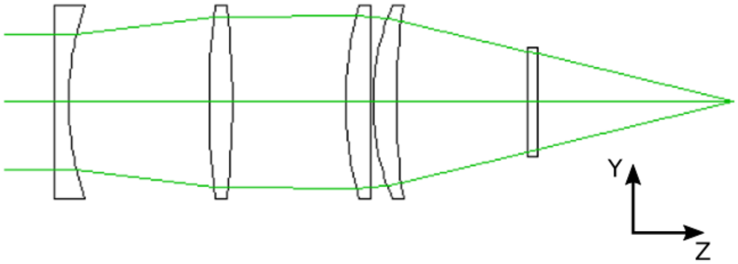

Figure 3.3: Lens Drawing: The system layout of the custom objective is shown with three rays traced from an on-axis point on the object located at ∞. The last optical element is an optically flat vacuum viewport window. The rays shown meet at the center of the vacuum chamber.

Graphical Ray Analysis

Figure 3.4 shows the spot diagram, at $\lambda = 532\,nm$, which results from tracing a large number of rays from a single on-axis object point through the system. The value of the *diffracton limit* is equal to the radius of the Airy disk and is shown by the solid black line. Since all of the input cone of rays originating from an on-axis object point, filling up the aperture, converge within the Airy Disk, we say that the system is diffraction limited. The values of the root-mean-square (RMS) sizes in different directions are also shown after a real ray trace is conducted through the system. For an ideal system free of aberrations, we would expect all rays to converge precisely at a single point.

Mathematically, we expect the intensity to be $\delta(\boldsymbol{r} = \mathbf{0})$. This is clearly not the case; the spot is *blurred* out because of the various imperfections present in the system which will be quantified in the next section.

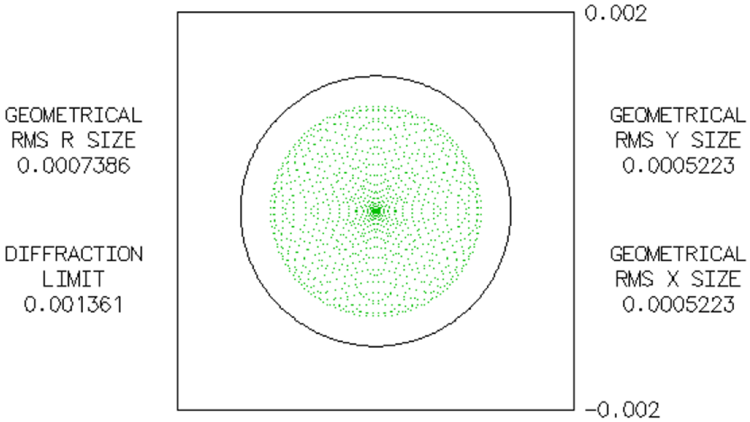

Figure 3.4: Spot Diagram: The green marks show the location of geometrical rays striking the image surface after originating from a uniformly illuminated on-axis object point while the black solid line delimits the diffraction limit of the custom objective. Since the system has an inherent cylinderical symmetry, the RMS spot sizes (diameter) in the X and Y directions are equal.

The RMS spot size (diameter) gives us a *rough* measure of the spread of the rays in which most of the energy is contained but this interpretation should only be taken with a grain of salt since almost never, in a lens design process, would one use the geometrical RMS size (diameter) to quantify the diffraction limited nature of the lens. As a matter of fact, the most useful analysis comes from the wavefront propagation methods through which we can obtain the MTF curves and the Point Spread Function (PSF). Nevertheless, we can understand the RMS spot size (diameter) mathematically using the concept of ray-displacements[3], ΔX and ΔY

$$\begin{aligned}\langle\sigma_x\rangle^2 &= \frac{1}{N}\sum_i^N(\Delta X_i - \langle x\rangle)^2\\ \langle\sigma_y\rangle^2 &= \frac{1}{N}\sum_i^N(\Delta Y_i - \langle y\rangle)^2\\ \langle\sigma_r\rangle^2 &= \langle\sigma_x\rangle^2 + \langle\sigma_y\rangle^2\end{aligned} \tag{3.4}$$

where

$$\langle x\rangle = \sum_i^N \Delta X_i$$

and similarly for $\langle y\rangle$. ΔX_i is the ray displacement[4] of the i^{th} ray traced. Ray displacements are used to quantify aberrations in an optical system. The values of $\{\sigma_x, \sigma_y, \sigma_r\}$ are shown in Figure 3.4 as geometrical RMS spot sizes (diameter).

Chromatic aberration finds its origin in the fact that the refractive index of glass $n(\lambda)$ varies with wavelength. This is called dispersion. The objective lens that I have designed is diffraction limited for both $461\,nm$ and $532\,nm$ but I did not achromatize the design which is done by using two different types of optical materials in the lens system. Therefore our system suffers from chromatic aberration. For the purposes of our experiment, we are only concerned with the *primary axial color* which is found, again using OSLO,

---

[3] Also called ray deviations, ray-intercepts or ray errors.

[4] The deviation of a traced ray from the reference ray where the reference ray is the ray which originates from the center of the object point and passes exactly through the center of the aperture stop.

to be $0.956\,mm$. Primary axial color (also called longitudinal chromatic aberration) is defined as the variation of the focal plane between the two wavelengths. Other chromatic aberration effects such as *lateral chromatic aberration*, which affects the magnification, and *secondary spectrum*, which is the residual chromatic aberration at $\lambda \neq 461\,nm \neq 532\,nm$, were not important for our experimental purposes and hence were ignored.

Transverse ray plots (also called ray-intercept curves) are used to summarize the performance of the lens and are particularly useful to identify specific types of aberrations that are manifestly undercompensated in an optical design. A detailed analysis of the ray trace curves is beyond the scope of this thesis however the interested reader is referred to [67, 68]. The ray intercept curves for our objective are shown in Figure 3.5. The three curves show the information for three arbitrarily selected object heights (field points in this case since the object is at ∞). The X axis labels the entrance pupil fractional coordinate while the Y axis is the ray displacement w.r.t the *chief ray*. The scale of the plots gives a quick idea of the amount of blurring that would take place for a particular object point. The ray intercept curve shown in Figure 3.5a is an S-shaped curve, which is typical of a system suffering from spherical aberration, with a maximum value of $\simeq 1\mu m$. It shows that for an axial point, the blur radius will have a magnitude of about 1 μm, in close agreement with the diffraction limit quoted earlier in Table 3.1. Its clear that the magnitude of the error increases for those rays passing closer to the edge of the entrance pupil's aperture. Indeed our design, at $\lambda = 532\,nm$ has residual spherical aberration for an on-axis object point. Notice also that for an axial point, the curve is always antisymmetric (odd function) since by definition, there is no astigmatism or coma for an on-axis point. For an off-axis point, a system suffering from pure coma would exhibit a characterstic U-shaped curve. Adding this U-shaped curve to the S-shaped spherical aberration curve produces an asymmetry in the spot diagram which is exactly what the ray-intercept curves in Figures 3.5b and 3.5c show, where one arm is elongated compared to the other. Therefore our system suffers from coma at larger field points, which correspond to larger deviations from the axial object point. This was demonstrated experimentally and will be illustrated in the next section (Figure 3.16).

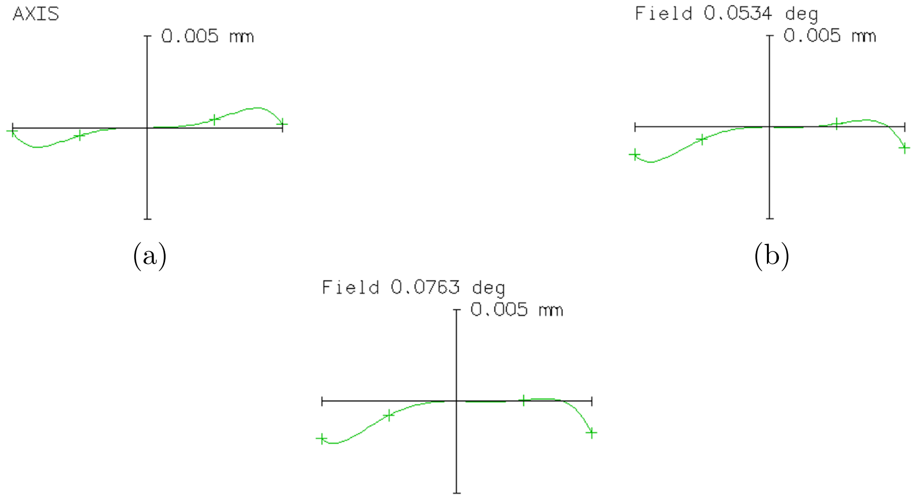

(a) (b)

(c)

Figure 3.5: Simulation of ray intercept curves for $\lambda = 532\,nm$, computed for various field points describing the types of aberrations affecting the quality of the diffraction limited spot. (a) Object is on on-axis. (b) Object is 70 μm off-axis along the Y axis. (c) Object is 100 μm off-axis along the Y axis.

Wavefront Anlaysis

Now, lets turn towards a more complete theory for the propagation of light which yields significantly more accurate results as compared to geometrical optics alone. Wave propagation is based on wavefronts, which are surfaces of constant phase. For a spherical wave, $\frac{e^{ikr}}{r}$, setting the argument of the exponential to a constant yields wavefronts as spherical surfaces. For every point on the image plane, there is a corresponding spherical wavefront converging to that point. This is how perfect image formation is described, for example, in the paraxial approximation. In a real system, the actual wavefront always deviates from this reference wavefront and this difference is quantified by the "Optical Path Difference" (OPD) or wavefront aberration, W_a. Figure 3.6 illustrates these concepts by showing the reference wavefront corresponding to a geometrically perfect point image. It can be seen from the figure that by retarding or advancing the ideal wavefront in a 2D plane, we can construct the real aberrated wavefront surface. This manifests itself as the optical phase difference of a scalar optical field : $e^{ik(r-W_a)}$.

It is useful to represent the wavefront in the form of polynomials, called *Zernike Polynomials*. (In principal we can choose any orthogonal set of polynomials but it turns out that the commonly observed aberrations in optical systems have an outstanding resemblance to the Zernike polynomials.) They form an orthogonal basis set in the 2D polar coordinates (ρ, θ) over a unit circle, where ρ is the radial coordinate while θ is the azimuthal angle. Denoting the i^{th} Zernike polynomial by $Z_i(\rho, \theta)$, the wavefront error can be written

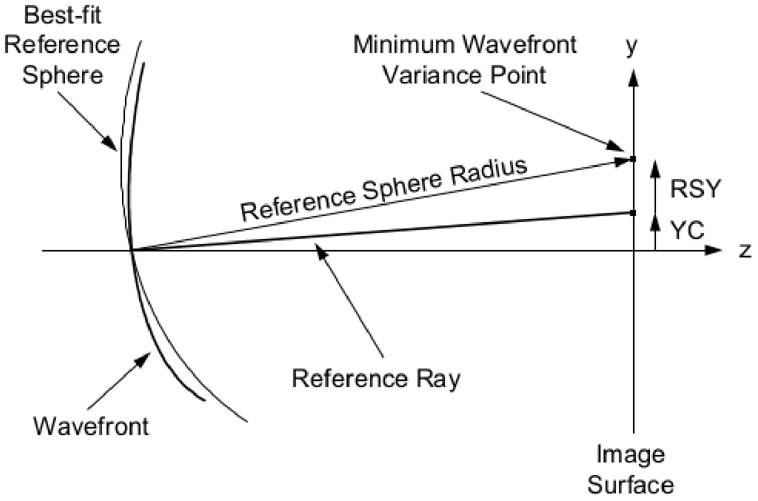

Figure 3.6: The figure shows the concept of the OPD using a hybrid picture between geometrical optics and wavefront propagation. The reference sphere corresponds to a wavefront converging to the ideal image point in the paraxial limit while the real wavefront is produced by including the effects of the aberrations. YC defines the actual location of the image while RSY is the ray displacement from the ideal. In the previous section, we saw plots of RSY which were called the ray intercept curves.

as [69]:

$$W(\rho, \theta) = \sum_{i=0}^{n} c_i Z_i(\rho, \theta) \tag{3.5}$$

where c_i are the aberration coefficients of the expansion. Different terms contribute different types of aberrations.

Now, lets talk about the Point Spread Function (PSF) of an optical system. It is interesting to note that, what a physicist calls the *Green's function* is the *impulse response* to an electrical engineer and the *point spread function* to an optical engineer. As was described in the previous chapter, the scalar electric field at the image plane can be computed using Fresnel diffraction equation (see Section 2.1) which is repeated here for convenience.

$$U(x', y') \propto \int_{-\infty}^{\infty} \int_{-\infty}^{\infty} P(x, y) \exp\left[i \frac{2\pi}{\lambda d}(xx' + yy')\right] \mathrm{d}x\mathrm{d}y \tag{3.6}$$

where (x, y) are the coordinates in the exit pupil (input transverse plane) and (x', y') are the image space coordinates (output transverse plane). The limits of integration are often set by the aperture of the exit pupil which is given by $P(x, y)$. For example, for a typical spherical lens, its a $circ(r)$ function. Notice that the double integral shown in the Equation (3.6) is essentially a 2D Fourier Transform of the aperture with frequency variables $v_x = \frac{x'}{\lambda d}$ and $v_y = \frac{y'}{\lambda d}$. This allows us to make use of the powerful tools of Fourier and linear systems theory. In particular, OSLO uses the 2D Fast Fourier Transfrom algorithm to compute this integral for a grid of points located in the object space. The PSF function is defined as the irradiance of the optical field at the image plane:

$$\mathrm{PSF}(x', y') = |U(x', y')|^2 \tag{3.7}$$

As shown in Figure 3.7, the PSF at both wavelengths resembles a typical Airy Disk intensity pattern. The diffraction limit and Airy disk radius are interchangeable terms and its values for both wavelengths are quoted in Table 3.1 but will be repeated here for convenience:

461 nm : $1.16\,\mu m$

532 nm : $1.36\,\mu m$

The Fourier Transform of the PSF is called the Optical Transfer Function (OTF) which measures the accuracy with which various frequency components in the object space are reproduced in the image. The OTF is in general a complex function and is defined as:

$$\mathrm{OTF}(v_x, v_y) = \frac{\displaystyle\int_{-\infty}^{\infty}\int_{-\infty}^{\infty}\mathrm{PSF}(x', y')\exp\left[i2\pi(v_x x' + v_y y')\right]\mathrm{d}x'\mathrm{d}y'}{\displaystyle\int_{-\infty}^{\infty}\int_{-\infty}^{\infty}\mathrm{PSF}(x', y')\mathrm{d}x'\mathrm{d}y'} \tag{3.8}$$

where I have normalized $\mathrm{OTF}(0, 0) = 1$. There are two general properties of the OTF:

1. $\mathrm{OTF}(-v_x, -v_y) = \mathrm{OTF}^*(v_x, v_y)$

2. $|\mathrm{OTF}(v_x, v_y)| \leqslant |\mathrm{OTF}(0, 0)|$

where * denotes the complex conjugate operation.

The OTF includes the effects of both geometric aberrations and diffraction and plays a key role in the assessment of image quality. We find that the OTF is identically zero for spatial frequencies larger than a certain value, the cutoff frequency v_0, which is given by

$$v_0 = \frac{2NA}{\lambda} \tag{3.9}$$

The magnitude of the OTF is called the Modulation Transfer Function (MTF) while the phase is called the Phase Transfer Function. The MTF

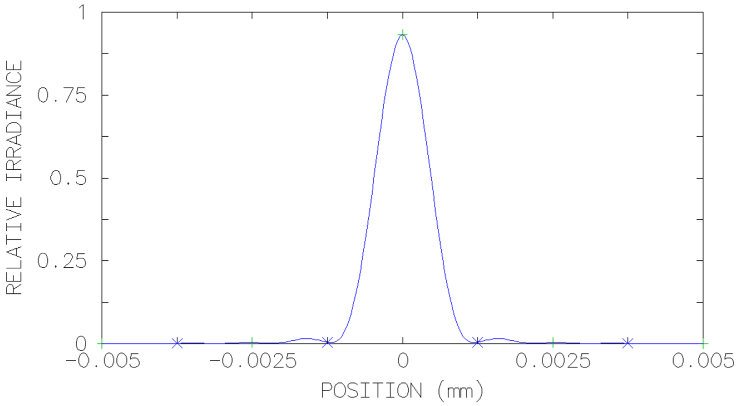

(a) 461 nm

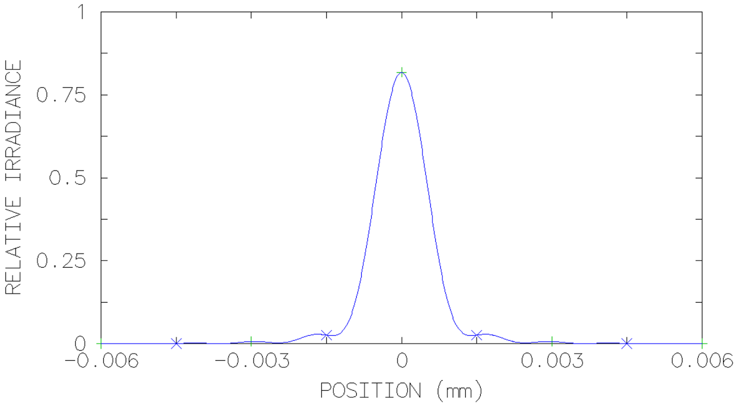

(b) 532 nm

Figure 3.7: PSF scans for an on-axis object point at the two design wavelengths. The PSF for 461 nm resembles the well-known Airy disk. The diffraction limit is the first minimum of the PSF which is numerically computed by OSLO in the spot diagram analysis Figure 3.4. Notice that the peak values are always less than 1 due to the presence of aberrations. This has important consequences when determining the diffraction-limited Field of View of the objective.

curves are densely packed with information which can be used to predict the performance of the optical system and many manufacturers provide them to showcase the performance of their design. A typical plot has *Modulation* on the y-axis while *spatial frequency* on the x-axis.

Modulation : Also called *modulation depth*[5] is defined in terms of the intensities as

$$M = \frac{I_{max} - I_{min}}{I_{max} + I_{min}} \tag{3.10}$$

and M $\in$ [0,1]. Its used interchangeably with the popularly known quantity, the *optical contrast.*

Spatial frequency : It is an alternate way to describe the resolution of an optical system. In particular, its inversely proportional to the resolution in μm:

$$\text{Res}(\mu m) = \frac{1}{2\,\text{Res}(lp/mm)} \tag{3.11}$$

where Res(μm) is approximately [6] equal to the diameter of the Airy Disk.

Figure 3.9 shows the MTF curve for our objective, computed in OSLO for $\lambda = 461\,nm$ at varying field points in the object space. The X axis labels the spatial frequency which is a measure of the ability of a lens system to resolve a pair of lines while the y axis labels the value of the MTF which

---

[5] Also called Michelson Contrast.

[6] It is *approximate* since spatial resolution uses an intensity square wave in the object plane while the Airy Disk is produced due to a circular flat top intensity profile in the object space.

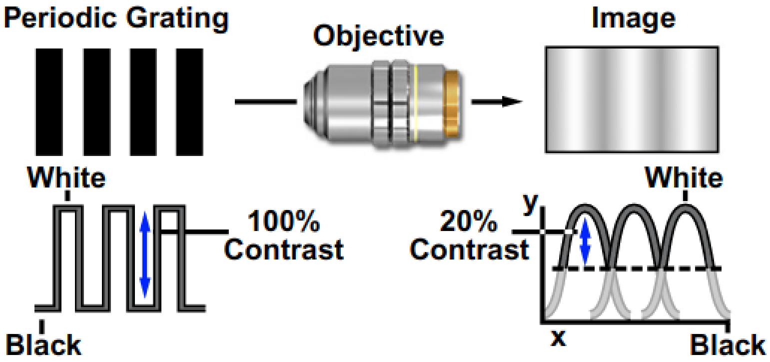

Figure 3.8: The figure illustrates the concept of contrast and how it applies to our test setup. The various sized objects in the 1951 USAF target serve the purpose of a periodic grating. The spreading or blurring of the grating after the objective is because of the convolution of the PSF with the periodic input intensity distribution which can be seen to be a train of rect(·) functions.

is proportional to the contrast. Recall that field points are used instead of object heights when the object is located at ∞, which is the case for our infinity-corrected objective. The on-axis curves have a higher contrast than the off-axis curves and going further away from the optical axis clearly degrades the contrast performance, as can be seen by comparing the blue and the green curves. Notice that all the curves only exhibit marginally lower contrast than an aberration-free lens (see ideal curve). The *modulation* (or contrast) is seen to decrease at higher spatial frequencies (which corresponds to smaller object sizes in μm). As the *modulation* decreases, it gets harder to resolve light originating from two object points placed close to each other Figure 3.8. Notice that a spatial resolution of $228.3\,\text{lp}/mm$ corresponds to a single rectangle of width $2.19\,\mu m$ which we experimentally resolved at $\lambda = 461\,nm$ as well as $\lambda = 532\,nm$ as shown later in Section 3.2. It is worth

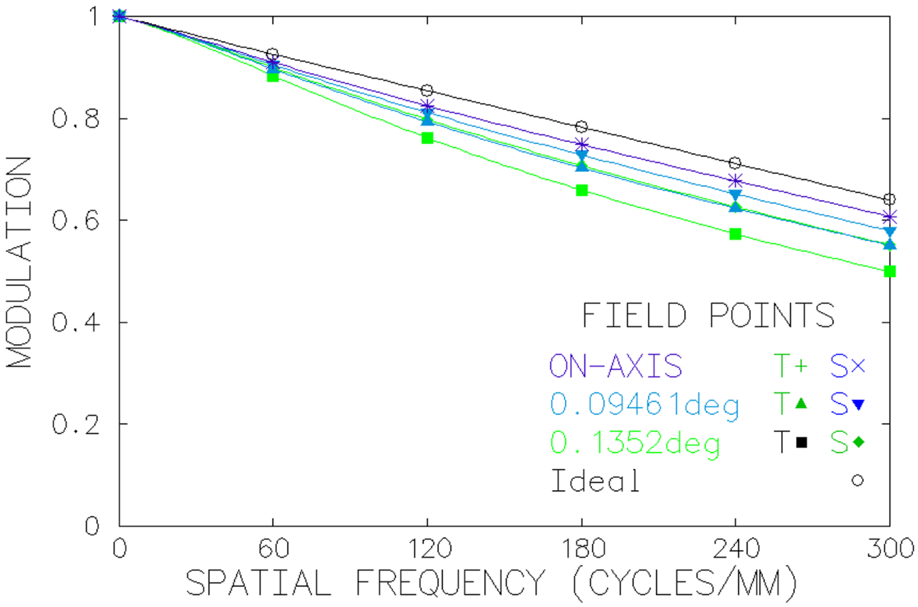

Figure 3.9: The MTF lens performance curve at $\lambda = 461\,nm$ computed by performing a 2D fft of the PSF for various field points. The solid black line represents the absolute theoretical limit of contrast for a system free of aberrations. For any real system, the curves must always lie below this limit. The analysis is done for three field points: 0.09461° representing 70% of the field, $123\,\mu m$ away from the optical axis, while 0.1352° is the curve at full field, $175\mu m$ away from the optical axis. T is for Tangential analysis while S is for Sagittal analysis.

noting in the figure above that the aberrations which cause asymmetry for off-axis object points, such as astigmatism, cause a difference in the contrast produced by the rays propagating in the tangential and sagittal planes.

Next, let's analyse the diffraction limited Field of View of the objective. This is important, for example, to calculate the maximum number of ODTs that can be imaged, with diffraction limited resolution, in a linear array. This gives us valuable information about how large of an optical tweezer array we can create during the experiment using the SLM. A widely used figure of merit to define the diffraction limited *field of view* (FOV) of an optical system is the region in which the *Strehl ratio* is greater than 0.8. The *Strehl ratio* is defined as the peak value of the actual PSF to the peak value of the an ideal PSF (without any aberrations). Referring back to Figure 3.7, its clearly seen that both PSFs have a peak value of less than 1 at the on-axis image space coordinate which agrees with the fact that our designed system is not ideal (ie paraxial regime is not enough). Using this criterion, I found the FOV for $\lambda = 461\,nm$ to be $400\,\mu m$ and at $\lambda = 532\,nm$ to be $210\,\mu m$.

3.1.3 How Does One Design a Lens: Optimization

Optimization referes to improving the performance of an optical system by varying certain parameters of the system iteratively. Typically these paramters are called "optimization variables" such as the radii of curvatures, element thicknesses, element-to-element separations and the optical glass types. All of these parameters can be controlled in the lens surface data spreadsheet shown in Table 3.4. The first step is to identify the constraints on the optical system which are usually imposed by the geometry of the environment in which the lens is going to be used. For example, for our experiment, a minimum working distance of $\sim 80\,mm$ was one of the constraints. Of course, image quality (characterized in terms of the Aberration coefficients) is another important criterion to achieve diffraction limited performance. In OSLO, these constraints are called *operands*. The system's performance is described quantitatively by a user-defined scalar *merit function* which is a weighted sum of the squares of the operands:

$$\phi(\boldsymbol{x}) = \sum_{i}^{m} w_i f_i^2 \tag{3.12}$$

where the vector $\boldsymbol{x}$ represents the set of optimization variables, f_i are the operands while w_i are the associated weights. Each component is written as the departure from a specific target value. There are many different optimization algorithms in use today. OSLO uses *Damped least squares optimization* which is specifically useful for nonlinear systems. For more information on how optimization is applied during the optical design process, please refer to [68, 69].

It is often useful to start with an existing design and in our case I used the first ever long working distance objective designed specifically for imaging atoms through a vacuum chamber [70]. Our goal was to design an infinity-corrected and diffraction limited objective, maximizing the numerical aperture given the minimum working distance imposed by the geometry of the vacuum viewport. It should come as no surprise that OSLO uses raytracing to compute the values of the operands and hence the merit function. The goal is to minimize the merit function in an N-dimension space where N is the number of variables (or parameters to be varied in the optical design). It is important to understand the topological nature of the merit-function space. There could be many local minima with several hills and valleys as

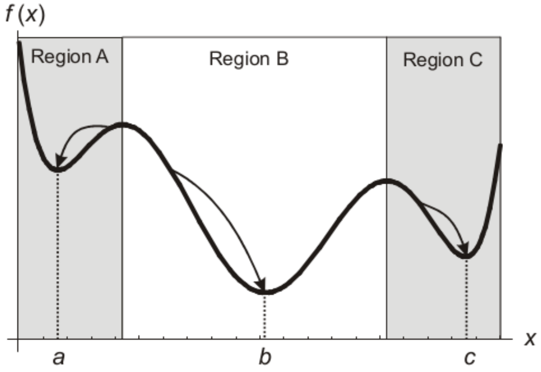

Figure 3.10: The figure shows a simplified 1D optimization topology with two local minima surrounding a global minimum. OSLO light is programmed to find local minima depending on the initial conditions used for designing the lens.

the parameters are varied. Each hill or valley may have smaller bumps and depressions which, to OSLO, would look like local minima and thus it would get stuck in that local minima which is certtainly a source of frustration for the optical designer. The minima we end up in depends on the initial values chosen by the lens designer. Therefore knowledge of existing lens designs can dramatically help in determining the right starting point which would eventually lead to diffraction limited performance. The global minima [71] is the bottom of the lowest valley (see Figure 3.10). Finding the global minima is a very computationally expensive process, not included in the OSLO Light version I used.

The whole idea of a multi-element objective lens is to compensate for the positive aberrations of convex surfaces with the negative aberrations of concave surfaces. As mentioned before the NA and the EFL were kept fixed which was easily achieved by allowing the radius of curvature of the last surface to vary during the optimization routine. The radii of curvature of the other seven surfaces, and their thicknesses were varied during the iterations. This gives us a $N = 8 + 4 + 3 = 15$ variables. The operands I used in the final stages of the optimization process and their corresponding weights are shown in Figure 3-11a. The operands were chosen to minimize the squared sum of all spherical aberrations up to 7th order and to minimize coma and astigmatism up to 3rd order. Figure 3-11b shows the iterations in one of optimization routines I ran in OSLO during the designing phase. Initially, I varied all 15 variables until diffraction limited performace was acheived given the contraints mentioned earlier. Once convergence was achieved, the first element was replaced with the closest 2" spherical lens available commercially (ThorLabs) and the program was allowed to re-optimize with N-3 variables thus reducing the dimensionality of the variable space. This process was repeated until all elements were commercial spherical singlets. It comes as no surprise that the final design looks remarkably similar to the one designed by W. Alt which suggests that these lens elements provide optimal aberration compensation for an optical system with the last element as a thin vacuum window. In addition, I had various special contraints for the optical design such as the minimum element-to-element spacing not drop below 0.50 mm to make it easy for the parts to be machined and device to be assembled.

It must be mentioned that designing a diffraction limited objective for two wavelengths without using two different types of glass elements is not as

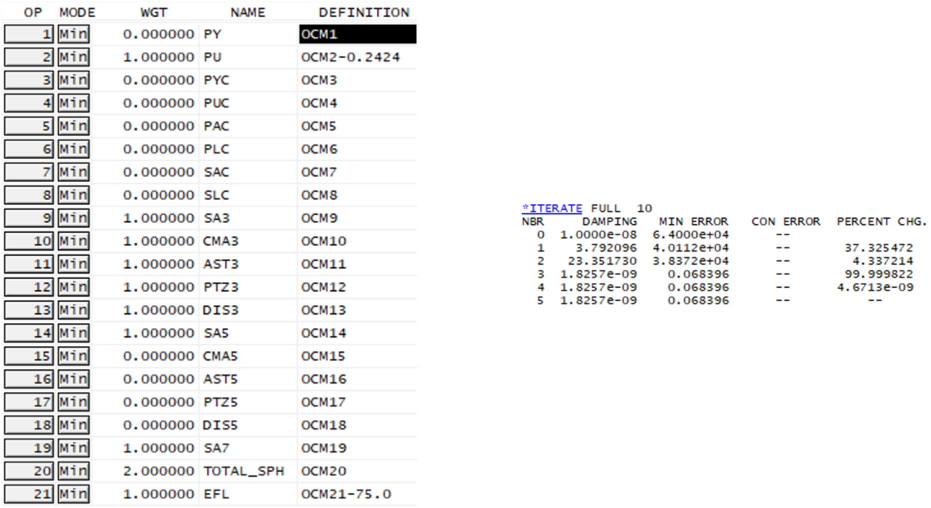

OP	MODE	WGT	NAME	DEFINITION
1	Min	0.000000	PY	OCM1
2	Min	1.000000	PU	OCM2-0.2424
3	Min	0.000000	PYC	OCM3
4	Min	0.000000	PUC	OCM4
5	Min	0.000000	PAC	OCM5
6	Min	0.000000	PLC	OCM6
7	Min	0.000000	SAC	OCM7
8	Min	0.000000	SLC	OCM8
9	Min	1.000000	SA3	OCM9
10	Min	1.000000	CMA3	OCM10
11	Min	1.000000	AST3	OCM11
12	Min	1.000000	PTZ3	OCM12
13	Min	1.000000	DIS3	OCM13
14	Min	1.000000	SA5	OCM14
15	Min	0.000000	CMA5	OCM15
16	Min	0.000000	AST5	OCM16
17	Min	0.000000	PTZ5	OCM17
18	Min	0.000000	DIS5	OCM18
19	Min	1.000000	SA7	OCM19
20	Min	2.000000	TOTAL_SPH	OCM20
21	Min	1.000000	EFL	OCM21-75.0

```
*ITERATE FULL  10
NBR      DAMPING   MIN ERROR    CON ERROR  PERCENT CHG.
  0   1.0000e-08  6.4000e+04       --
  1     3.792096  4.0112e+04       --        37.325472
  2    23.351730  3.8372e+04       --         4.337214
  3   1.8257e-09    0.068396       --        99.999822
  4   1.8257e-09    0.068396       --       4.6713e-09
  5   1.8257e-09    0.068396       --           --
```

Figure 3.11: Optimization was perfomed using OSLO's built in damped least square optimiztion algorithm. (a) While setting up the operands, some were assigned a higher weight while for certain others the weight was set to 0. OSLO is programmed to minimize each array labelled OCMx to 0 hence for example, at the end of the optimization process, the value of PU should be close to 0.2424. (b) Shows the iterations during performed for a single optimization run. The damping factor is dynamically changed to vary the size of the jump in the N dimensional optimization space during each iteration. The "MIN ERROR" is the $\phi(\boldsymbol{x})$ as described in Equation (3.12) and is minimized iteratively.

straightforward as running the optimization procedure for one of the two wavelengths. Instead of choosing either of the two wavelengths, I used $\lambda = 515\,nm$ which served as a sweet spot between the two required design wavelenghts. As seen in the previous section, the Strehl ratio at $532\,nm$ drops below 0.8 faster than for $461\,nm$ which causes the FOV to be different at the two wavelenghts. As seen from the detailed performance analysis described in the previous section using simulations in OSLO, it is clear that the lens design was prioritized for the imaging wavelength $461\,nm$ rather than the trapping wavelength 532 nm.

3.1.4 Looking Out for Manufacturing Errors: Tolerance Analysis

Since we designed and built the objective lens ourselves in house, it was critical to understand how machining and assembly errors would affect the overall performance of the system. OSLO uses both Monte-Carlo methods and the method of Finite Differences to estimate how various errors in the spacings, radii of curvatures, tilts and decentrations of various lens surfaces would affect an arbitrarily set merit function including, but not limited to, the RMS spot size (diameter), wavefront error, MTF or the boresight error. In what follows, I analyse the effect of deviations of element to element thickness by using the method of finite differences.

The only parameter under our control is the element to element separation because all other parameters such as element thicknesses and errors in the radii of curvatures of the lenses had standard tolerances provided by ThorLabs. In the OSLO light version, I merely had access to the *sensitivity analysis* and *inverse sensitivity analysis*. The first step in such analyses is to define a merit function. I chose the merit function to be the error function generated earlier during the optimization process since it captures all the relevant performance measures of an aberration-free objective lens. In a typical sensitivity analysis, a set of parameters are deviated from their ideal value (one at a time) and the change in the merit function is computed. This gives us a clear picture of the worst offenders ie which parameters affect the performance the most. In this way, I can assign a tighter tolerance to that particular parameter. In an inverse sensitivity analysis, a maximum allowed value for the change in the merit function is arbitrarily selected, and subsequently the tolerance limit for each parameter is found individually. The result of both of these analyses is shown in the Figure 3.12.

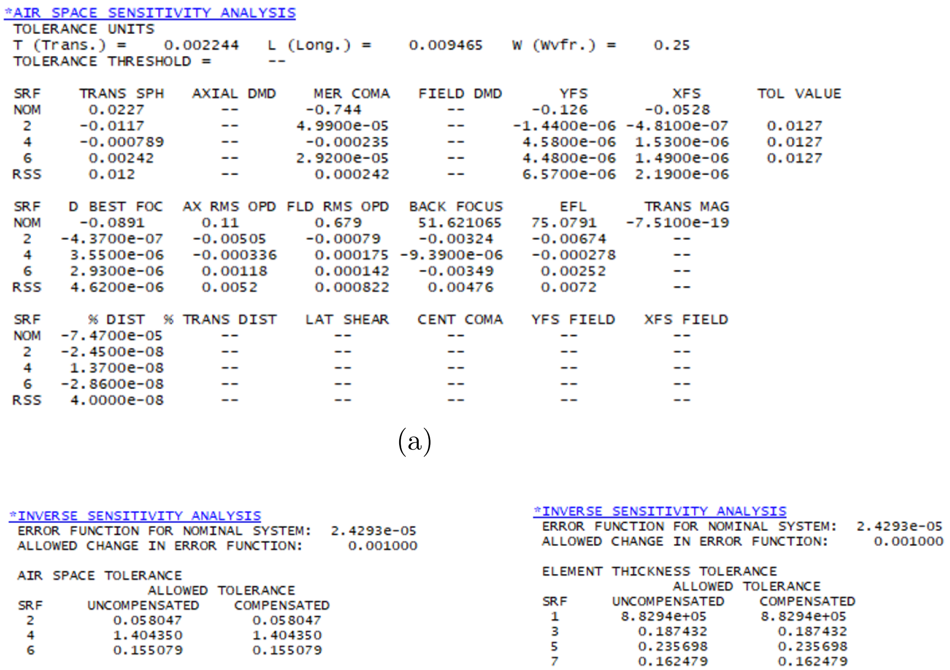

```
*AIR SPACE SENSITIVITY ANALYSIS
 TOLERANCE UNITS
 T (Trans.) =     0.002244   L (Long.) =     0.009465   W (Wvfr.) =     0.25
 TOLERANCE THRESHOLD =       --

 SRF     TRANS SPH    AXIAL DMD     MER COMA     FIELD DMD        YFS          XFS        TOL VALUE
 NOM      0.0227         --          -0.744          --          -0.126       -0.0528
  2      -0.0117         --        4.9900e-05        --       -1.4400e-06 -4.8100e-07    0.0127
  4      -0.000789       --         -0.000235        --        4.5800e-06  1.5300e-06    0.0127
  6       0.00242        --        2.9200e-05        --        4.4800e-06  1.4900e-06    0.0127
 RSS      0.012          --          0.000242        --        6.5700e-06  2.1900e-06

 SRF    D BEST FOC   AX RMS OPD  FLD RMS OPD  BACK FOCUS       EFL       TRANS MAG
 NOM     -0.0891        0.11         0.679      51.621065    75.0791    -7.5100e-19
  2    -4.3700e-07   -0.00505      -0.00079     -0.00324    -0.00674        --
  4     3.5500e-06   -0.000336      0.000175  -9.3900e-06   -0.000278       --
  6     2.9300e-06    0.00118       0.000142    -0.00349     0.00252        --
 RSS    4.6200e-06    0.0052        0.000822     0.00476     0.0072         --

 SRF      % DIST   % TRANS DIST    LAT SHEAR    CENT COMA    YFS FIELD    XFS FIELD
 NOM   -7.4700e-05      --            --           --           --           --
  2    -2.4500e-08      --            --           --           --           --
  4     1.3700e-08      --            --           --           --           --
  6    -2.8600e-08      --            --           --           --           --
 RSS    4.0000e-08      --            --           --           --           --
```

(a)

```
*INVERSE SENSITIVITY ANALYSIS
 ERROR FUNCTION FOR NOMINAL SYSTEM:   2.4293e-05
 ALLOWED CHANGE IN ERROR FUNCTION:      0.001000

 AIR SPACE TOLERANCE
                    ALLOWED TOLERANCE
 SRF       UNCOMPENSATED      COMPENSATED
  2           0.058047          0.058047
  4           1.404350          1.404350
  6           0.155079          0.155079
```

(b)

```
*INVERSE SENSITIVITY ANALYSIS
 ERROR FUNCTION FOR NOMINAL SYSTEM:   2.4293e-05
 ALLOWED CHANGE IN ERROR FUNCTION:      0.001000

 ELEMENT THICKNESS TOLERANCE
                    ALLOWED TOLERANCE
 SRF       UNCOMPENSATED      COMPENSATED
  1         8.8294e+05        8.8294e+05
  3           0.187432          0.187432
  5           0.235698          0.235698
  7           0.162479          0.162479
```

(c)

Figure 3.12: A typical result of tolerancing analysis in OSLO. (a) Shows the sensitivity analysis performed by varying the element spacings, as the parameters, while subsequently computing the error in various merit functions. (b & c) Show the results of inverse sensitivity analysis for the element spacings and element thicknesses. The computation was done for $\lambda = 532\,nm$.

The minimum tolerance possible for the spacers was $12.7\mu m$ for the machinist on campus. A sensitivity analysis was performed Figure 3.12a and the errors in various merit functions were computed. The "TOL VALUE" represents the quoted value of the machinist's tolerance in *mm*. The three spacings are represented by surfaces 2-6 (as described earlier in table 3.4). The values given in the figure are in *tolerance units* given at the top of the figure for various types of merit functions. The RSS value is the *root-sum-squared* value very similar to the commonly used RMS value. The values in the figure clearly show that almost all the important merit functions such as FLD RMS OP (RMS wavefront error), EFL, DIST (distrotion) etc are all orders of magnitude smaller than their NOM (nominal) values. In Figure 3.12b, I show the tolerance limit of the spacings to keep the change in the error function less than 1x10^{-3} in absolute terms. Figure 3.12c shows the tolerance limit of the element thicknesses to keep the change in the error function less than 1x10^{-3}. The tolerance limits obtained are clearly much larger than our machining precision which shows that our design is robust against nominal machining errors.

Note that I performed a manual tolerancing analysis of all spacings at their tolerance limits. This gives us a more realistic case where errors are introduced in the system simultaneously. To perform a complete analysis in which all variables of the lens are varied randomly, following a certain probability distribution (usually gaussian), Monte Carlo analysis must be performed especially because the variables in a typical lens design can be large in number. Since I only had access to the OSLO light version, I did not have the luxury to do such an analysis.

3.2 Lens Performance Evaluation

In this section I shall describe the lens assembly procedure I used and the measures I took to ensure that the objective remained within the tolerance limits. After the assembly of the lens, ex vacuo tests were performed on the objective using the smallest objects I could find in the lab including the 1951 USAF target, the tip of a *single mode fiber* (SMF) and the focus of a commercial 10X microscope objective of NA = 0.25. This gives us a range of objects with varying sizes and shapes and, as we shall see in the results that follow, the objective lens performed in close agreement with the predictions of OSLO within the limits of experimental accuracy. I measured the FOV as well as the PSF of the objective for both $\lambda = 461\,nm$ and $\lambda = 532\,nm$. The test setup employed, as shown in Figure 3.13, was a relay telescope consisting of the objective lens in conjunction with an $f = 1000\,mm$ spherical singlet. This sets the primary magnification of the complete optical system to be -13.3. Note that since the objective lens is designed to work alongside the optically flat vacuum viewport, I used an exact replica of the vacuum viewport installed in our actual vacuum chamber. The image was formed on a CMOS ThorLabs DCC1545M monochrome USB 2.0 camera which has a pixel size of $5.2\,\mu m$ corresponding to an effective pixel size of $391\,nm$ in the

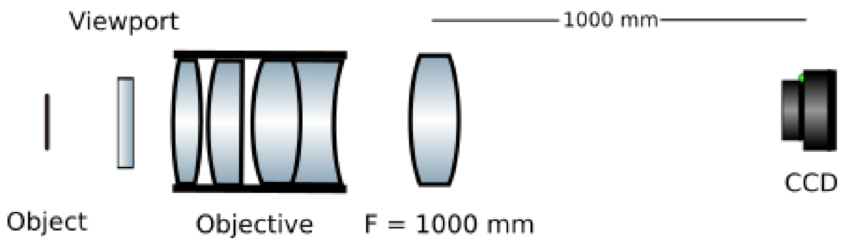

Figure 3.13: The optical schematic of the test setup used for all the experimental tests performed on the objective lens. Various types of objects were used including the 1951 USAF target, the tip of a SMF and the focus of a commercial microscope objective.

object plane.

3.2.1 Lens Assembly

After doing a thorough tolerance analysis detailed in the previous section, I ensured that the tilts and displacements were kept within limits. The displacements were kept within the tolerance limits by high precision machining with tight mechanical tolerances ($12.7\,\mu m$) for the designed spacers which separate the lens elements. The elements are precisely placed on-axis inside a threaded standard lens tube (ThorLabs SM2L30) which was modified to accomodate the full 3.5" length of the designed objective. The lenses were dropped in one element at a time, the lens tube nudged each time to ensure the lens was sitting flat inside the tube. In addition, to minimize the tilts, firstly I made the spacers *press-fit* with the internal diameter of the lens tube and secondly, the spacers were designed in such a way that they contacted each element exactly $2.54\,mm$ from the outer edge. This way I avoided the chamfers which were a possible source of error and would violate the tolerance limits set by the analysis done in the previous section. The slope of the spacer was matched to the slope of each spherical surface at the point of contact to within 0.1° accuracy. The drawing files of the spacers have been attached in Appendix B.

3.2.2 Diffraction-Limit and Field Of View

The simplest test which gave us an estimate of resolution of the optical system was to use the 1951 USAF target which hosts a precise assortment of spatial frequencies. The spatial frequency, as defined in Equation (3.11), is inversely related to the width of a single rectangle in the test target. The target was placed on a transverse translation stage (X-Y axes) and was back illuminated with a collimated gaussian beam at $\lambda = 461\,nm$ and separately for $\lambda = 532\,nm$. The laser source at $\lambda = 461\,nm$ was fibered into a $10\,m$ long fiber (ThorLabs P3-405BPM-FC-10) and subsequently collimated using a triplet collimator. Figure 3.13 shows the experimental test setup used while Figure 3.14 shows the results obtained.

The PSF can be obtained experimentally by fitting a rectangular pulse convolved with the PSF to the image profile. This is because the PSF is the impulse response of a linear optical system. Using the concepts from linear systems theory, given the impulse response and the input, we can therefore find the output intensity of a linear optical system as:

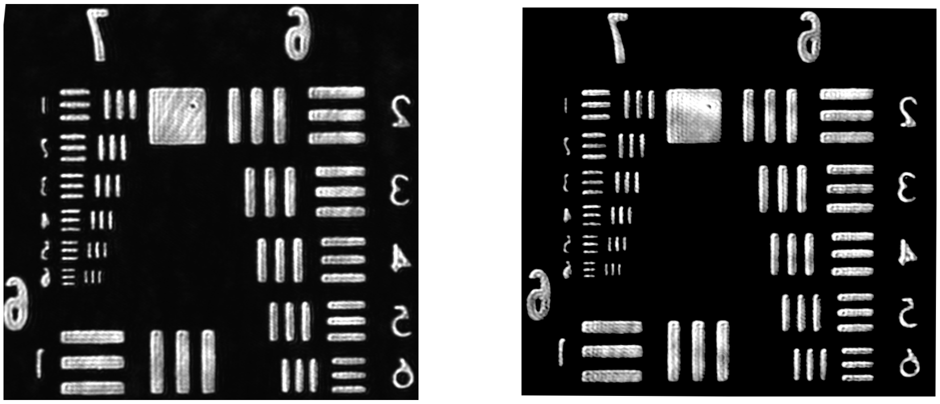

(a) 461 nm

(b) 532 nm

Figure 3.14: Experimentally imaging the 1951 USAF target at the two design wavelengths. Groups 6 and 7 are shown and are clearly resolvable. This suggests that the resolution of this optical system is better than 2.19 μm which corresponds to the 6th element of group 7.

$$\tilde{I}(x', y') = \int_{-\infty}^{\infty} \mathrm{PSF}(x - x', y - y') I(x, y) \mathrm{d}x \, \mathrm{d}y \tag{3.13}$$

The equation above is the convolution between the PSF and input intensity profile. In words, this means that each point in the object plane produces a PSF in the image plane. A weighted sum of these PSFs over the entire object space, generates the final intensity distribution in the image plane with the weights being proportional to the local emittance of the point object. The computed value of the Airy Disk radius for $\lambda = 532\,nm$ is found to be $1.47 \pm 0.11\,\mu m$ which is in close agreement to the theoretically predicted value from OSLO. Note that we need not care about interference effects since the the object is assumed to be incoherent which would be the case, for example, when imaging single Rydberg atoms trapped in an optical tweezer array. Next, I used a commercial 10x microscope objective from Spencer with a NA = 0.25 to create a single tightly focused Gaussian spot which was subsequently imaged by the custom objective. Again, using the theory of wave-propagation, the image is the result of the convolution of the PSF with gaussian intensity distribution which gave us a slightly different answer for the Airy Disk radius at $\lambda = 532\, nm$ as 1.58 $\pm 0.09\, \mu m$.

To test the predicted values of the FOV of the objective lens, we raster-scanned the tip of a SMF across the FOV of the objective by a manual translation stage (X-Y). The first step was to ensure that the SMF was approximately close to the optical axis which was achieved experimentally by taking multiple horizontal scans (along the X axis) for each value of Y. The value of Y corresponding to the largest FOV along the horizontal axis was set as the Y coordinate of the optical axis. The process was repeated for the X axis and in this way we found the (X-Y) coordinates of the optical axis of the system at the plane of the SMF. During each scan, we took more than 40 images with a spatial step resolution of $50\, \mu m$. The resulting images were fitted with a 2D gaussian function and the $\frac{1}{e^2}$ radius was plotted by averaging the values from the X and Y slices obtained. Figure 3.15 shows the experimentally computed FOV for both wavelengths of interest.

Note that sometimes an alternate definition is used to define the FOV as the circle inside which the spot size (diameter) is within $\sqrt{2}$ times the on-axis spot size (diameter). We used a more restrictive and stricter definition of the FOV diameter. The FOV was determined as the diameter of the circle where

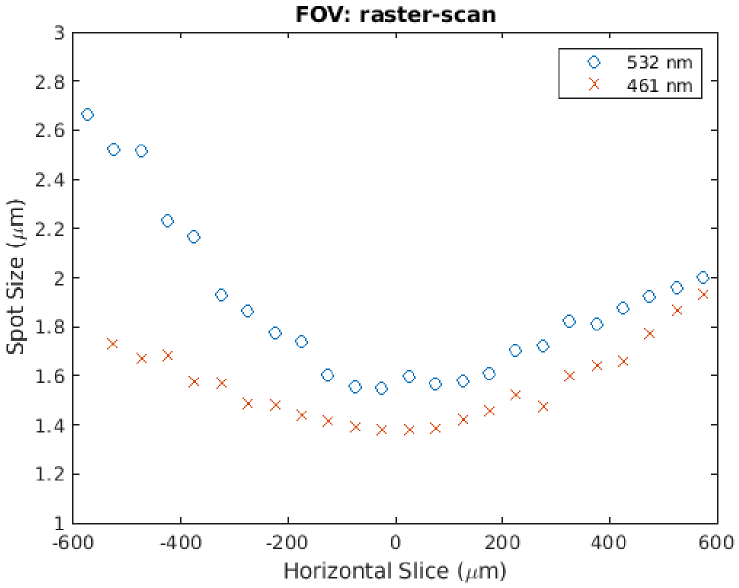

Figure 3.15: Measuring the FOV of the objective lens by scanning the tip of a SMF mounted on a two-axis translation stage. The region where the spot size is approximately constant is defined as the diffraction limited FOV of the objective.

the spot size (diameter) remained within 5% of the minimum on-axis value. For $\lambda = 461\,nm$ it was found to be $350\,\mu m$ and for $\lambda = 532\,nm$ it was found to be $300\,\mu m$. Notice that there are two reasons for the difference in the spot sizes (diameters) for the two wavelengths: i) the airy disk radius is larger for $\lambda = 532\,nm$ and ii) the mode field diameter of fiber is smaller at $\lambda = 461\,nm$. The asymmetry in the direction of the raster scan is caused because of a minor tilt of the objective lens w.r.t the fiber. Imaging the SMF outside the FOV, we observed severe coma such that the spot size (diameter) increased along one axis more than the other, asymmetrically. This is illustrated in Figure 3.16.

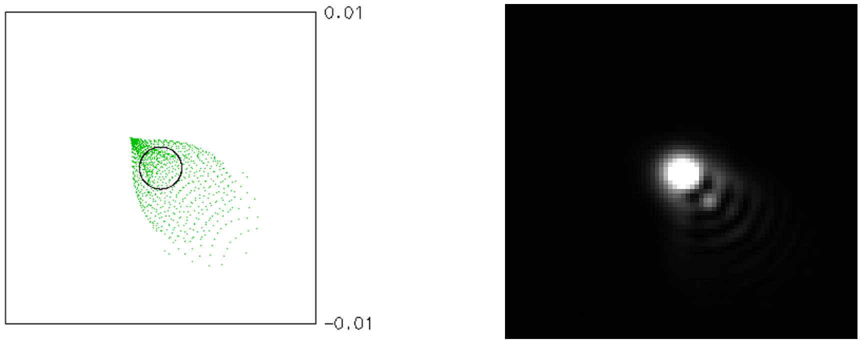

(a) (b)

Figure 3.16: An exagerrated illustration of imaging a SMF outside the diffraction-limited FOV of an objective lens using $\lambda = 532\,nm$. (a) Shows the simulation results when a point object is $495\,\mu m$ away from the optical axis (at 45°). (b) Shows the experimental image of the SMF, $500\,\mu m$ away from the optical axis of the objective.

It is important for us to characterize the chromatic shift between the two design wavelengths for our objective lens. This was found for all testing configurations described above and was measured to be $0.965\,mm$, in close agreement with the theorectically predicted value of $0.96\,mm$ by OSLO.

3.3 Summary

In conclusion, I have presented the design of a custom, low-cost, long-working distance, microscope objective lens, consisting four spherical singlet elements, which is to be used in conjunction with a standard optical vacuum viewport. After a gentle introduction to some important concepts necessary to work with OSLO, I described the step-by-step process of optimization including the selection of variables as degrees of freedom, and operands as important performance metrics of the lens system. Simulations were performed in OSLO to show the diffraction limited nature of the objective which were subsequently validated by ex vacuo experimental testing using numerous standard objects including the 1951 USAF target and the tip of a SMF. It is worth mentioning a few additional groups which have successfully attempted to design their own objective lenses: 1) Mark Saffman's group [72] and 2) Lincoln Turner's group [73]. It is important to state that this design can be made to be accomodate other wavelengths by simply achromatizing the design with the use of two different types of glass materials. The design process is general and can be optimized for diffraction-limited monochromatic fluorescence imaging at the D_2 line of alkali metals such as the $780\,nm$ $5\,S_{\frac{1}{2}}$ to $5\,P_{\frac{3}{2}}$ transition in Rb or the $852\,nm$ $6\,S_{\frac{1}{2}}$ to $6\,P_{\frac{3}{2}}$ transition in Cs and has been explicitly demonstrated in [73].

Chapter 4

Final Experimental Characterization

Here I shall describe the final optical layout which has been successfully built and tested ex-vacuo. It combines the high-resolution imaging with the beam shaping setup to give our group the ability to perform a vast range of experiments exploiting the tremendous control and precision associated with the SLM as well the custom designed objective. Here is a brief description of the optics used:

- F_1 : Thorlabs AL50100G-A 100 mm Asphere. Mounted on a flipper mount
- F_3 : 400 mm Planoconvex lens used to expand the output SLM beam
- F_4 : 125 mm Planoconvex lens used to expand the output SLM beam

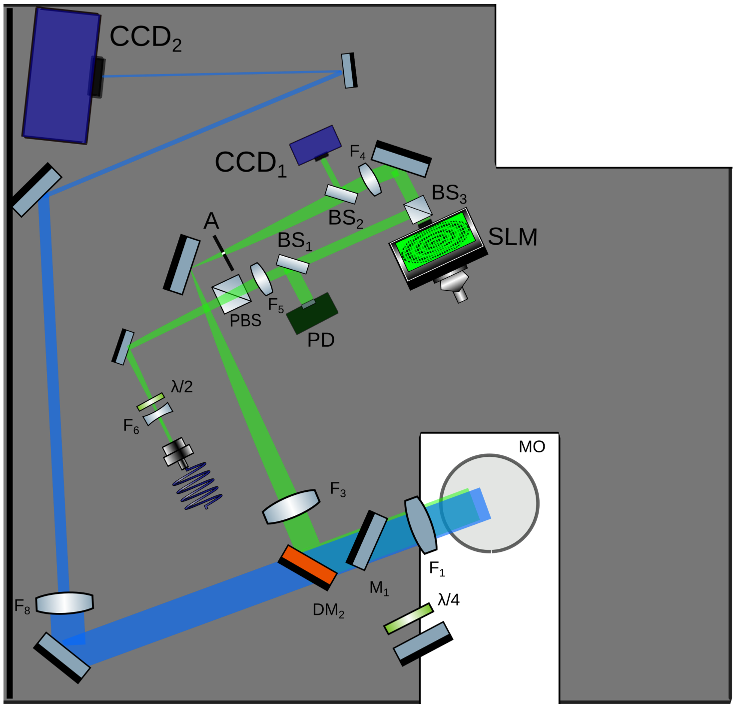

Figure 4.1: The final optical layout of system. It shows the green beam at $\lambda = 532\,nm$ which is first expanded after undergoing phase modulation due to the SLM and, is then directed through the objective to create extremely tight ODTs. Also shown is the blue fluorescence which is collected and collimated by the custom-designed objective lens and is subsequently imaged by the 1000 mm lens onto the sensor plane of CCD_2.

- F_5 : 150 mm Planoconvex lens used to expand the input SLM beam
- F_6 : -15 mm Biconcave lens used to expand the input SLM beam
- F_8 : Biconvex 1000 mm Imaging lens
- BS_1: Beam sampler for monitoring and controlling the power in the traps
- BS_2: Beam sampler for observing the images of the trap on the diagonostic CCD
- BS_3: Beam splitter (50:50) used to re-direct the reflected beam off the SLM
- PBS : Polarizing beam splitter used to improve the horizontal polarization quality input to the SLM
- M_1 : Broadband dielectric mirror mounted on a flipper mount
- DM_1: ThorLabs DMLP567L long pass dichroic mirror (not shown in the schematic)
- DM_2 : ThorLabs DMSP490L short pass dichroic mirror is used to separate the trapping beam with the imaging beam.
- PD : Photo-diode to measure the power in the beam and feedback to the AOM. (not shown)
- MO : Custom designed microscope objective lens

- A : Aperture

Since we plan to install the objective vertically (thus imaging the planes parallel to the optical table), this sytem had to take into account the two MOT beams: $461\,nm$ and the $689\,nm$. The $461\,nm$ beam is responsible for the blue MOT and was described in detail in Camargo's thesis [74] while the $689\,nm$ is used during the second stage of the laser cooling process to create the red MOT and was described in Ding's thesis [75]. To separate out the different optical beams, necessitates the need for DM_1 (not shown in the optical schematic). In addition, since the imaging beam obtained by fluorescence as well as the red-detuned trapping beam at $\lambda = 532\,nm$ share the same path through the objective, it was important to add a second dichroic mirror DM_2.

The aspheric lens F_1 collimates the upward travelling MOT beam after it passes through the objective lens. The mirror M_1 and the aspheric lens F_1 are mounted on a flipper mirror mount (ThorLabs MFF102) thus while the MOT is being created, it is not possible to image or create the ODTs. It takes around $0.8s$ for the flipper mirror to switch position from one state to another. The path of the MOT beam at $\lambda = 461\,nm$ goes through $F_1 \rightarrow M_1 \rightarrow \frac{\lambda}{4}$ and back onto itself via retro-reflection (since opposite circularly polarized beams of light travelling antiparallel to each other are required to create a MOT). We used an asphere to collimate the light from the strongly focusing MOT beam after the objective to ensure better collimation quality for the retro-reflection. An exactly similar setup was employed for the red at $\lambda = 689\,nm$

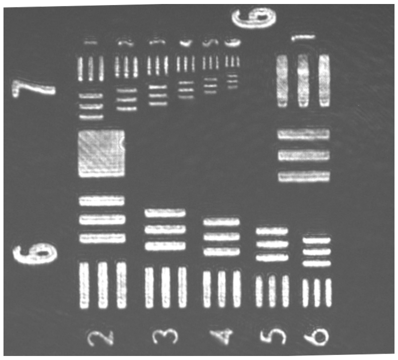

Figure 4.2: Imaging the 1951 USAF with all optics in their final positions. The vacuum viewport (not shown) was included in between the objective and the target since the objective performs optimally alongside the viewport.

beam which is not shown in the schematic since it lies symmetrically on top of the microscope objective in a plane perpendicular to the optical layout.

After building the final optical system, a quick test of resolution was performed using the 1951 USAF as before for the $\lambda = 461\,nm$ and Figure 4.2 shows that all objects were resolvable suggesting that the system is performing as expected. The smallest object $[Group\,7, Element\,6]$ is resolvable which contains rectangles of size of $2.2\mu m$.

4.1 Long Range, High Resolution Axial Imaging

An additional requirement explored in the final setup was the ability to vary the imaging plane for the $\lambda = 461\,nm$. One obvious way to do that is to physically move the objective but since the MOT beams pass through

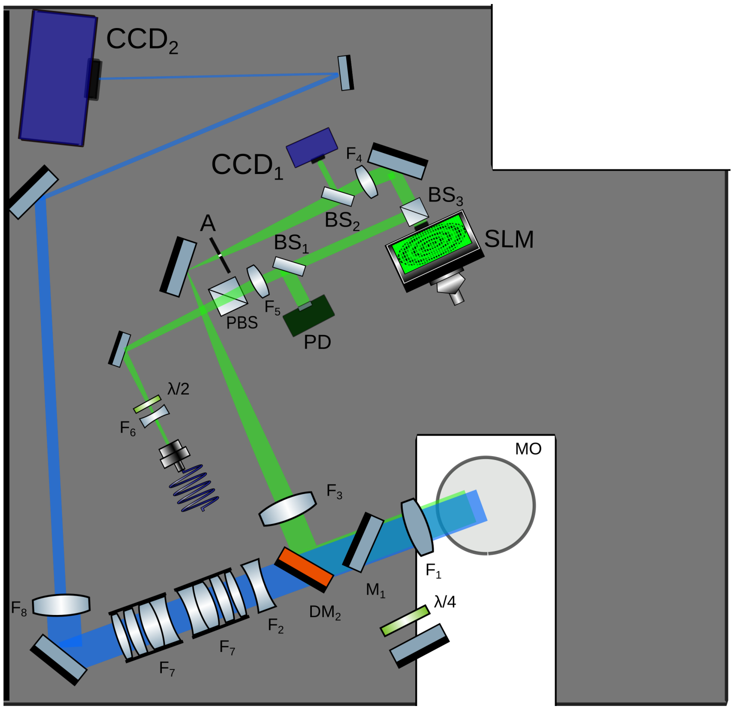

Figure 4.3: Three additional lens elements are included in the fluorescence imaging beam path. For an incoming collimated beam, the lens F_2 creates a magnified virtual image (inside the vacuum chamber). The lenses F_7 are commercial imaging lenses of fixed focal length which can image objects between $300\,mm$ and ∞ away from its last surface.

the objective, that would affect the re-collimation of the MOT beams and thus cause uneven forces along the vertical axis. This is undesirable since it would shift the location of the center of the MOT away from the center of the vacuum chamber and thus the null of the magnetic field. Therefore we employed a different solution which is described in Figure 4.3.

- F_2 : -500 mm biconcave lens
- F_7 : Edmund Optics 50 mm fixed focal length lens (Stock# 63-248)

For a $0\,mm$ shift in the focal plane, the lens F_2 creates a magnified virtual image (inside the vacuum chamber) which is then imaged by F_7 onto a plane exactly in the middle of the two commercial fixed focal length lenses labeled F_7. This is a real image and is created by the first commercial lens F_7. The second commercial lens then collimates this beam. This process utilizes an intermediate imaging plane while maintaining a sufficiently high resolution. Note that since the overall fluorescence imaging path is no longer infinity corrected, the additional elements introduce unknown aberrations into the imaging path thus the image quality is slightly degraded. In addition, the action of variable focus causes the magnification to vary for each individual shift in the focal plane. In the following section, I shall explore both of these effects on our imaging system and quantify the shift in magnification as well as the degradation in the imaging resolution.

On the contrary, to image an object in a plane shifted by, lets say $3\,mm$, (away from the focal plane of the objective), a virtual image is formed *farther away* (as compared to the location of the original virtual image) and the fixed focal length lenses is adjusted to focus this virtual image onto the plane exactly in the middle of the lenses labeled F_7. The second F_7 lens is always set to ∞ because it simply serves to collimate the beam (ie form the image at ∞).

Figure 4.4 shows an image of the fixed focal length lens (on our custom C-mount). As mentioned previously, the lens can be adjusted to focus objects at variable distances onto a single imaging plane and the markings

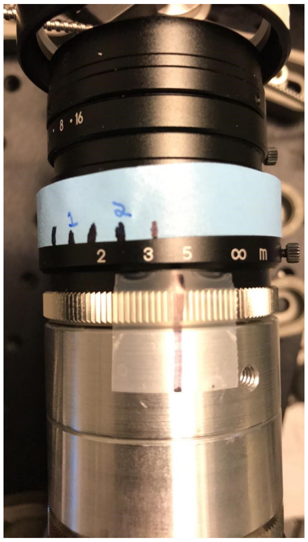

Figure 4.4: The commercial fixed focal length imaging lens set to $F/\# = 1.4$ is used to vary the imaging plane by upto $5\,mm$.

corresponding to various shifts in the imaging plane are shown. The imaging performance was characterized by using the 1951 USAF target and the results for various focal shifts are shown in Figure 4.5. Clearly the imaging performance is not the same as obtained without the the three extra optical elements in the imaging path in Figure 4.3.

4.2 Magnification Analysis

To analyze the contrast, we take a single object (for example the horizontal bars in Element 5) and integrate it along the horizontal axis to obtain a better signal to noise level. The data was then fitted by a Gaussian $I(r) = I_0\, exp\left(\frac{-2r^2}{w^2}\right)$ to obtain the values of w for different objects selected from the

(a) No additional lenses

(b) 0 mm

(c) 0.5 mm

(d) 1.0 mm

(e) 1.5 mm

(f) 2.0 mm

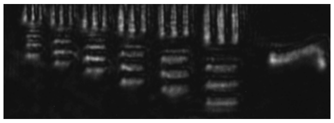

(g) 2.5 mm

Figure 4.5: Shows the effect of varying the imaging plane on the resolution test target. (a) Shows the image obtained without any additional lens elements in the imaging path. [(b)-(g)] Show the images obtained on the CCD as the target was placed at increasing distances from the focal plane of the objective. Only Group 7 is considered.

1951 USAF target at various magnitudes of shifts in the imaging plane[1].

The images used for the analysis are the various elements in group 7. The horizontal bars are selected for each element, integrated along the horizontal axis and a curve fitting code in MATLAB is run to find the location of the peaks of three Gaussians along a vertical slice. The three Gaussians are constrained to be of the same width. This process is illustrated in Figure 4.6.

The most important parameters obtained from the Gaussian fit are the

---

[1] There is a slight error in this process since, ideally, we should have fitted the data with the PSF convolved with a $rect(\cdot)$ as done in the previous chapter.

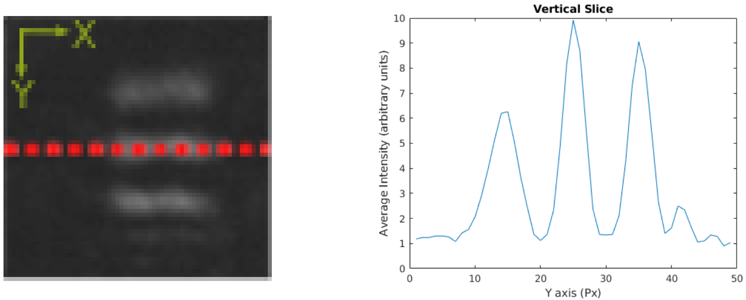

(a)

(b) 0 mm

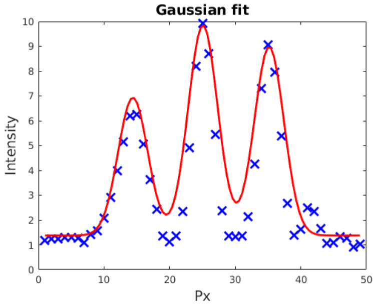

(c) 0 mm

Figure 4.6: (a) Shows a typical object in the target. Integration is performed over the red dotted line (along the X axis) to assign an average value to every pixel along the Y axis. (b) Resulting integrated signal as a function of pixels along the Y axis. (c) Shows the resulting gaussian fit obtained.

locations of the peaks of the curves which will help us obtain the width of each rectangle using the symmetrical nature of the three rectangles in the target. Its important to note that we are not using the width of the Gaussian to determine the size of the rectangles since doing so results in an underestimated value.

The graph in Figure 4.7 shows the results obtained after analyzing the magnification of all six elements in group 7 of the 1951 USAF target. The red curve shows the average magnification of the six objects for every value of

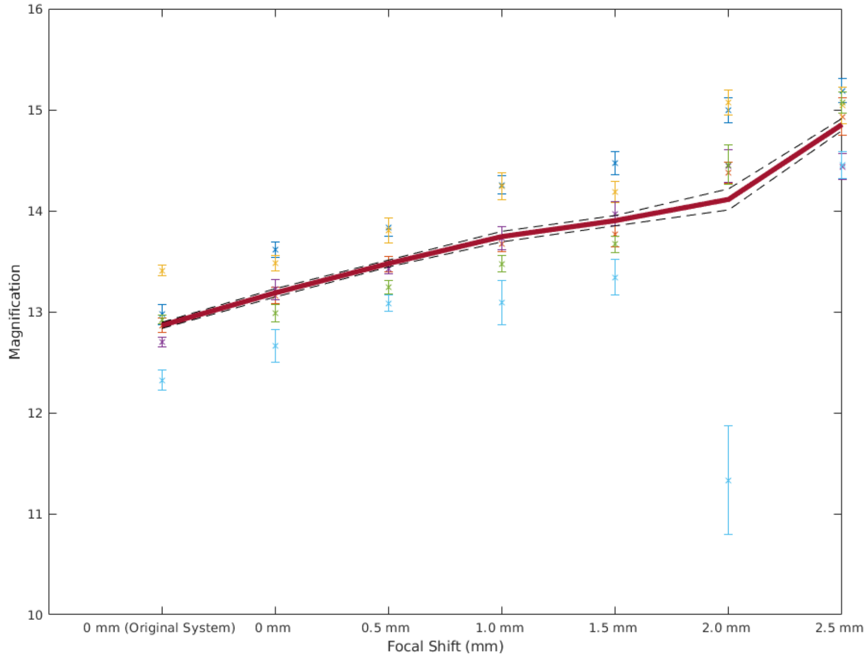

Figure 4.7: Results obtained for the magnification for every element in Group 7. The sizes of the object are known while the sizes of the images are computed by using Gaussian curve fitting analysis. The average magnification is shown as well as the standard deviation in the computed value of M.

shift (in the imaging plane) and the black dotted line shows the uncertainty bounding the calculation.

Appendices

Appendix A

MATLAB code

For an updated copy of the working code along with sample phase profiles and a detailed overview of wave propagation, please refer to:
https://github.com/KillianRice/SLM-code

A.1 Generating phase profiles

A.1.1 Basic Functions

```
function [ x,n ] = unitstep_dt( n1,n0,n2 )
    %UNITSTEP_DT Summary of this function goes here
    %   Detailed explanation goes here
    n = n1:n2;  %the time vector
    n0 = find(n == n0); % finds the index of the step starting point
    x = zeros(1,length(n));
    x(n0:end) = 1;
end
```

```
function [ y,ny ] = shift( x, nx,n0 )
    %SHIFT Summary of this
```

```
    function goes here
    %   y[n] = x[n-n0]
    ny = nx + n0;
    y = x;
end
```

```
function [ y,ny ] = fold( x, nx )
    %FOLD Summary of this function goes here
    %   Detailed explanation goes here
    ny = fliplr(-nx);
    y = fliplr(x);

end
```

A.1.2 Grating profile and 3D translation

```
%% The purpose of this piece of code is to generate a phase profile using prism and lens phase (in the image plane).
close all;
clear all;
clc;

%% System Parameters
w_beam  = 0.535e-3;    % beam waist of the generated mode
lambda  = 532e-9;      % illumination wavelength
k = 2*pi/lambda;       % Wave number
dx = 12.5e-6;          % Pixel Pitch of Hamamatsu SLM (X13138-04) aka sampling freq
D = pwd;               % Working Directory of this file
f = 1000e-3;          % focal length : 1000 mm lens

%% Options
saveFile = 1;  % options are: ’1’ or ’0’

%% Creating a 2-D Mesh
Ncols = 1272;
Nrows = 1024;

```

```
xx = 1:Ncols;
yy = 1:Nrows;
[x,y] = meshgrid(xx,yy);


%% Grating profile
% (must be even number for periodicity in discrete time)
T_x = 50;                         % period of the grating in terms of pixels X axis
T_y = 50;                         % period of the grating in terms of pixels Y axis

[n_x,Sp_x] = my_square(Ncols,T_x);
[n_y,Sp_y] = my_square(Nrows,T_y);

% Uncomment to add another frequency grating
% (must be even number for periodicity in discrete time)
Tx_highfreq = 100;                % period of the grating in terms of pixels in X axis
Ty_highfreq = 100;        % period of the grating in terms of pixels in Y axis
[n_x,Spx_highfreq] = my_square(Ncols,Tx_highfreq);
[n_y,Spy_highfreq] = my_square(Ncols,Ty_highfreq);
Ax_highfreq = 0;
Ay_highfreq = 0;
Spx_highfreq = Spx_highfreq * Ax_highfreq;
Spy_highfreq = Spy_highfreq * Ay_highfreq;

% Amplitude (remember, max value is pi)
A_x = pi;
A_y = 0;
Sp_x = Sp_x * A_x;
Sp_y = Sp_y * A_y;

%% Generating Phase Patterns
```

```
( all phase is in range [0,2 pi) )

% Grating profile
Phi_grating_x = zeros(1024,1272);
Phi_grating_highfreq_x= zeros(1024,1272);
Phi_grating_y = zeros(1024,1272);
Phi_grating_highfreq_y = zeros(1024,1272);

% multiplying the square wave with the matrix to create a matrix with a
% square wave
for iter_col = 1:1272
    for iter_row = 1:1024
        Phi_grating_x(iter_row,iter_col) = Sp_x(iter_col);          %high freq x
        Phi_grating_highfreq_x(iter_row,iter_col) = Spx_highfreq(iter_col); % low freq x
    end
end
for iter_row = 1:1024
    for iter_col = 1:1272
        Phi_grating_y(iter_row,iter_col) = Sp_y(iter_row);  % high freq y
        Phi_grating_highfreq_y(iter_row,iter_col) = Spy_highfreq(iter_col); % low freq y
    end
end

% Adding phase profiles moduli 2 pi
Phi_grating = mod(Phi_grating_x + Phi_grating_y + Phi_grating_highfreq_x + Phi_grating_highfreq_y,2*pi);
figure('Name','Grating Phase Profile','NumberTitle','off');
```

```
imshow(Phi_grating,[0 2*pi]);
colorbar;

% Shift in longitudinal direction
Phi_lens = mod(-k*(dx)^2/(2*f)*((x-Ncols/2).^2+(y-Nrows/2).^2),2*pi);
figure('Name','Fresnel-Lens Phase Profile (ColorMap)','NumberTitle','off');
imshow(Phi_lens,[0,2*pi]);
colorbar;

% Shift in the transverse direction (blazed grating or prism phase)
a = 1e-3;
Phi_prism = mod(-a*k*x*dx,2*pi);
figure('Name','Prism Phase Profile (ColorMap)','NumberTitle','off');
imshow(Phi_prism,[0,2*pi]);


% Sinusoidal Phase Grating

c = 2*pi;              % contrast
period_px = 100;       % period in terms of pixels
f_0 = 1/(dx*period_px);    % spatial frequency of the grating
phi_sin = c/2 * sin(2*pi*f_0*x*dx)+c/2;
figure('Name','Sinusoidal grating Phase Profile (ColorMap)','NumberTitle','off');
imagesc(phi_sin/pi);
colormap gray;
h = colorbar;
ylabel(h,'\phi (units of \pi)');
axis off;


%% Final Kinoform: (for computation)
% Note: All computation is done in double precision. This is important. If
```

```
% I do the computation in 8 bit numbers, significant errors are introduced.
% Results were compared.
Phi_total = mod(Phi_prism + Phi_lens + Phi_grating+ phi_sin,2*pi);
figure('Name','Total Phase Total_Phase_Profile_computat','NumberTitle','off');
imshow(Phi_total,[0,2*pi]);

Phi_total = 255/(2*pi) * Phi_total;          % Converting from [0,2pi] to [0,255]

%% Final kinoform: (for displaying onto SLM)
% Wavefront Correction:
S = fullfile(D,'Kinoforms','CAL_LSH0802080_532nm.bmp');
wvf_cor_532 = imread(S);
wvf_cor_532 = double(wvf_cor_532);
Phi_slm = mod(Phi_total + wvf_cor_532,256);
% Note: According to the Inspection sheet of the SLM. For 532 nm, at signal 210,
% we get 2 pi phase modulation. Thats how the SLM twisted nematic crystals
% are operating at 532 nm at room temperature.
Phi_slm = Phi_slm*210/255;
% Appending zeros (because SLM ignores the last 8 columns)
Z = zeros(1024,8);
Phi_slm = cat(2,Phi_slm,Z);
figure('Name','Total_Phase_Profile_SLM','NumberTitle','off');
imshow(Phi_slm,[0 255]);

%% Saving File (using 8-bit numerics)

% Saving file
if saveFile == 1
```

```
  Phi_slm = uint8(Phi_slm);
  Phi_total = uint8(Phi_total);
  imwrite(Phi_slm,'Total_Phase_Profile_SLM.bmp','bmp');
  imwrite(Phi_total,'Total_Phase_Profile_computat.bmp','bmp');
end
```

A.1.3 Damman Grating

I present the code for two optimized Damman grating profiles to generate 8 and 13 equal intensity spots in 1D. The phase profile is then extended to 2D to generate 64 and 169 equal intensity spots, respectively.

```
%Binary phase grating with translational symmetry producing odd number of
%spots: 13
clear all;
close all;

N = 2048;   %Size of image will still be 1024 x 1272
x_axis = 1:N;
T = 256;
%% Transition points obtained after optimization
x_n = [0.1289 0.3233 0.5862 0.6139 0.7290 0.7919 0.9074]; % transitions
x_n_T = round(x_n*T) + 1;                           % rounded off to integer
phi_n = [0,pi,0,pi,0,pi,0,pi];
n = 1:T;

% 1st
[y1,n] = unitstep_dt(n(1),1,n(end));
[y2,n] = unitstep_dt(n(1),x_n_T(1)+1,n(end));
F0 = phi_n(1)*(y1-y2);

% 2nd
[y1,n] = unitstep_dt(n(1),x_n_T(1),n(end));
```

```
[y2,n] = unitstep_dt(n(1),
    x_n_T(2),n(end));
F1 = phi_n(2)*(y1-y2);

% 3rd
[y1,n] = unitstep_dt(n(1),
    x_n_T(2),n(end));
[y2,n] = unitstep_dt(n(1),
    x_n_T(3),n(end));
F2 = phi_n(3)*(y1-y2);

% 4th
[y1,n] = unitstep_dt(n(1),
    x_n_T(3),n(end));
[y2,n] = unitstep_dt(n(1),
    x_n_T(4),n(end));
F3 = phi_n(4)*(y1-y2);

% 5th
[y1,n] = unitstep_dt(n(1),
    x_n_T(4),n(end));
[y2,n] = unitstep_dt(n(1),
    x_n_T(5),n(end));
F4 = phi_n(5)*(y1-y2);

% 6th
[y1,n] = unitstep_dt(n(1),
    x_n_T(5),n(end));
[y2,n] = unitstep_dt(n(1),
    x_n_T(6),n(end));
F5 = phi_n(6)*(y1-y2);

% 7th
[y1,n] = unitstep_dt(n(1),
    x_n_T(6),n(end));
[y2,n] = unitstep_dt(n(1),
    x_n_T(7),n(end));
F6 = phi_n(7)*(y1-y2);

% 8th
[y1,n] = unitstep_dt(n(1),
    x_n_T(7),n(end));
F7 = phi_n(8)*y1;
%% Finaly phase profile
F = F0 + F1 + F2 + F3+ F4+ F5
    +F6+F7;
figure('Name','Single period'
    ,'NumberTitle','off');
plot(n/T,F/pi);
ylabel('\phi (units of \pi)')
    ;
axis([0 inf -0.5 1.5]);

```

```
rep = N/T;                  % Number of repitions
func = repmat(F,1,rep);     % Repeating one period

figure('Name','Damman Grating Phase Profile (1D)','NumberTitle','off');
plot(x_axis,func/pi);
axis([0 N -0.5 1.5]);
xlabel('Pixels');
ylabel('\phi (units of \pi)');
clearvars -except func N x_axis

%% extending to 2D

for iter_col = 1:1272
    for iter_row = 1:1024
        Phi_x(iter_row,iter_col) = func(iter_col);          %high freq
    end
end
for iter_row = 1:1024
    for iter_col = 1:1272
        Phi_y(iter_row,iter_col) = func(iter_row);
    end
end
figure('Name','Damman Grating Phase Profile (2D)','NumberTitle','off');
Phi = mod(Phi_x+Phi_y,2*pi);
imagesc(Phi/pi,[0 2]);
colormap gray;
h = colorbar;
ylabel(h,'\phi (units of \pi)');
axis off;
%% Saving the 2D file as .bmp (8 bit)

Phi = 255/(2*pi) * Phi;         %Converting from [0,2pi] to [0,255]
Phi = uint8(Phi);
imwrite(Phi,'Dammann_2D_phase_13.bmp','bmp');
```

```
%Binary phase grating with translational symmetry
```

```
producing even number of
%spots: 8
close all;
clear all;

N = 2048;      %Size of image will still be 1024 x 1272
x_axis = 1:N;
T = 512;
%% Transition points obtained after optimization
x_n = [0.1812,0.2956,0.3282,0.4392, 0.5000,0.6812,0.7956,0.8282, % transitions
x_n_T = round(x_n*T) + 1;          % rounded off to integer
phi_n = [0 pi 0 pi 0 pi 0 pi 0 pi];
n = 1:T;

% 1st
[y1,n] = unitstep_dt(n(1),1,n(end));
[y2,n] = unitstep_dt(n(1),x_n_T(1)+1,n(end));
F0 = phi_n(1)*(y1-y2);

% 2nd
[y1,n] = unitstep_dt(n(1),x_n_T(1),n(end));
[y2,n] = unitstep_dt(n(1),x_n_T(2),n(end));
F1 = phi_n(2)*(y1-y2);

% 3rd
[y1,n] = unitstep_dt(n(1),x_n_T(2),n(end));
[y2,n] = unitstep_dt(n(1),x_n_T(3),n(end));
F2 = phi_n(3)*(y1-y2);

% 4th
[y1,n] = unitstep_dt(n(1),x_n_T(3),n(end));
[y2,n] = unitstep_dt(n(1),x_n_T(4),n(end));
F3 = phi_n(4)*(y1-y2);

% 5th
[y1,n] = unitstep_dt(n(1),
```

```
    x_n_T(4),n(end));
[y2,n] = unitstep_dt(n(1),
    x_n_T(5),n(end));
F4 = phi_n(5)*(y1-y2);

% 6th
[y1,n] = unitstep_dt(n(1),
    x_n_T(5),n(end));
[y2,n] = unitstep_dt(n(1),
    x_n_T(6),n(end));
F5 = phi_n(6)*(y1-y2);

% 7th
[y1,n] = unitstep_dt(n(1),
    x_n_T(6),n(end));
[y2,n] = unitstep_dt(n(1),
    x_n_T(7),n(end));
F6 = phi_n(7)*(y1-y2);

% 8th
[y1,n] = unitstep_dt(n(1),
    x_n_T(7),n(end));
[y2,n] = unitstep_dt(n(1),
    x_n_T(8),n(end));
F7 = phi_n(8)*(y1-y2);

% 9th
[y1,n] = unitstep_dt(n(1),
    x_n_T(8),n(end));
[y2,n] = unitstep_dt(n(1),
    x_n_T(9),n(end));
F8 = phi_n(9)*(y1-y2);


% 10th
[y1,n] = unitstep_dt(n(1),
    x_n_T(9),n(end));
F9 = phi_n(10)*y1;
%% Finaly phase profile
F = F0 + F1 + F2 + F3+ F4+ F5
    +F6+F7+F8+F9;
figure('Name','Single period'
    ,'NumberTitle','off');
plot(n/T,F/pi);
ylabel('\phi (units of \pi)')
    ;
axis([0 inf -0.5 1.5]);

rep = N/T;
              % Number of repitions
func = repmat(F,1,rep);
              % Repeating one period

figure('Name','Damman Grating
     Phase Profile (1D)','
```

```
    NumberTitle','off');
plot(x_axis,func/pi);
axis([0 N -0.5 1.5]);
xlabel('Pixels');
ylabel('\phi (units of \pi)')
    ;
clearvars -except func N
    x_axis
%% extending to 2D
for iter_col = 1:1272
     for iter_row = 1:1024
          Phi_x(iter_row,
    iter_col) = func(iter_col)
    ;           %high freq
     end
end
for iter_row = 1:1024
     for iter_col = 1:1272
          Phi_y(iter_row,
    iter_col) = func(iter_row)
    ;
     end
end

figure('Name','Damman Grating
     Phase Profile (2D)','
    NumberTitle','off');
Phi = mod(Phi_x+Phi_y,2*pi);
imagesc(Phi/pi,[0 2]);
colormap gray;
h = colorbar;
ylabel(h,'\phi (units of \pi)
    ');
axis off;
%% Saving the 2D file as .bmp
     (8 bit)
Phi = 255/(2*pi) * Phi;
        %Converting from [0,2pi
    ] to [0,255]
Phi = uint8(Phi);
imwrite(Phi,'
    Dammann_2D_phase_8.bmp','
    bmp');
```

A.2 Wave propagation

Wave propagation is performed by implementing the Fresnel Diffraction integrals as a Fourier transform. The first two subsections show the computation done in rectangular coordinates for the most general optical beam profiles. If a beam is cicrularly symmetric, we can convert to polar coordinates and reduce the 2D fourier transform to a 1D Hankel transform which is an integral over the radial coordinate only. This approach is particularly useful for gaussian beams or other circulary symmetric beams like the well-known Laguerre-Gaussian beam modes.

A.2.1 1D

```
close all;
clear all;
clc;

%% Setting up system parameters

s_factor = 1;          % Set this to 1 for default (actual) values. Set this to larger than 1 for scaling the fft2. This ...
                       % ...will introduce increasing errors as you increase its value largr.
Lambda = 532e-9;     % Wavelength
k = 2*pi/Lambda;     %Wave number
f_fourier = (400)*1e-3; % Focal length of the Fourier Transforming Lens
dx = s_factor*12.5e-6; % spatial period of sampling (pixels)
F_s = 1/dx;   %spatial freq of sampling (pixels)
N = 1024;
x = [-N/2:1:N/2-1];


%% Input phase profile here: (example of sinusoidal grating shown)
% other 1D phase profiles of length 1024 can be
```

```
included
c = 2*pi;            % contrast
period_px = 50;       % period in terms of pixels
f_0 = 1/(dx*period_px);   % spatial frequency of the grating
phi_sin = c/2 * sin(2*pi*f_0*x*dx)+c/2;
figure('Name','Sinusoidal grating Phase Profile (ColorMap)','NumberTitle','off');
imagesc(phi_sin/pi);
colormap gray;
h = colorbar;
ylabel(h,'\phi (units of \pi)');
axis off;


xx = dx*(-N/2:1:N/2-1); % The x axis
x = exp(i*phi_sin);   % The electric field

% Plotting the Phase profile in 1D
figure('NumberTitle','off','Name','1D Computation: Fourier Transform');
s(1) = subplot(2,2,1);
plot(xx,angle(x)/pi);
ylabel('Phase \Phi (units of \pi)');
xlabel('X axis');
s(2) = subplot(2,2,2);
plot(xx,abs(x));
ylabel('Amplitude');
xlabel('X axis');
title(s(1),'Phase profile SLM plane');
title(s(2),'Amplitude profile SLM plane (normalized)');
%% Computing the Fresnel Diffraction Integral
FFT = fft(x,N);
y = fftshift(FFT);

% Setting the axis
w_freq = linspace(-pi,pi-(2*pi)/N,N);
```

```
freq_proper = F_s*w_freq/(2*pi);          %Spatial frequency
clear x;
x = freq_proper*Lambda*f_fourier;        % converting from spatial frequency to coordinates

% Plotting the Image plane Field
s(4) = subplot(2,2,4);
plot(s_factor*x/(1e-3),abs(y));
ylabel('Amplitude');
xlabel('X axis (mm)');
s(3) = subplot(2,2,3);
plot(s_factor*x/(1e-3),angle(y));
ylabel('Phase \Phi (units of \pi)');
xlabel('X axis (mm)');
title(s(3),'Phase profile Image plane');
title(s(4),'Amplitude profile Image plane');
```

A.2.2 2D

```
% This piece of code can take a phase profile and give you the resulting
% electric field in the fourier plane.

close all;
clear all;
clc;
%% Setting up system parameters

s_factor = 1;        % Set this to 1 for default (actual) values. Set this to larger than 1 for scaling the fft2. This ...
                     % ...will introduce increasing errors as you increase its value largr.

D = pwd;               % Working Directory of this file
Lambda = 532e-9;    %
```

```
Wavelength
k = 2*pi/Lambda;     %Wave number
f_fourier = 77e-3; %Focal length of the Fourier Transforming Lens
T_s = s_factor*12.5e-6; % spatial period of sampling (pixels)
F_s = 1/T_s;   %spatial freq of sampling (pixels)

%% Reading image file and converting to proper phase scaling

S = fullfile(D,'Dammann_2D_phase_8.bmp'); %input the phase profile
Phi = imread(S);
% Phi = Phi(:,:,1);
Phi = 2*pi/255 * double(Phi);
Phi = Phi(:,1:1272);
figure('NumberTitle','off','Name','2D Computation: Fourier Transform');
s(2) = subplot(2,2,2);
imshow(Phi,[0 2*pi]);
title(s(2),'Input Phase profile');

%% Generating 2D Eletric Field
Ncols = 1272; % X axis
Nrows = 1024; % Y axis

xx = T_s*(-Ncols/2:1:Ncols/2-1);
yy = T_s*(-Nrows/2:1:Nrows/2-1);

u_amp = 1;
u = exp(i*Phi);

s(1) = subplot(2,2,1);
imagesc(xx,yy,u_amp);
xlabel('X_{SLM} axis');
ylabel('Y_{SLM} axis');
title(s(1),'Amplitude profile SLM plane (normalized)');


%% The Fourier transform (2D)
% The electric field in the
```

```
   Fourier plane
v = fft2(u);
v = fftshift(v);

% Axes
w_freq_cols = linspace(-pi,pi
   -(2*pi)/Ncols,Ncols);
freq_proper_cols = F_s*
   w_freq_cols/(2*pi);
    % Spatial frequency
x_cols = freq_proper_cols*
   Lambda*f_fourier;       %
   converting from spatial
   frequency to coordinates

w_freq_rows = linspace(-pi,pi
   -(2*pi)/Nrows,Nrows);
freq_proper_rows = F_s*
   w_freq_rows/(2*pi);
    % Spatial frequency
x_rows = freq_proper_rows*
   Lambda*f_fourier;       %
   converting from spatial
   frequency to coordinates

% Display image

s(3) = subplot(2,2,3);
imagesc(s_factor*x_cols/(1e
   -3),s_factor*x_rows/(1e-3)
   ,abs(v).^2);
title(s(3),'Amplitude profile
    Image plane');
xlabel('X_{image} (mm)');
ylabel('Y_{image} (mm)');
```

A.2.3 Circular Symmetry

Please refer to: https://github.com/KillianRice/SLM-code

A.3 GS Algorithm

Please refer to: https://github.com/KillianRice/SLM-code

Bibliography

[1] Mark Saffman, Thad G Walker, and Klaus Mølmer. “Quantum information with Rydberg atoms”. In: *Reviews of modern physics* 82.3 (2010), p. 2313.

[2] Mark Saffman. “Quantum computing with atomic qubits and Rydberg interactions: progress and challenges”. In: *Journal of Physics B: Atomic, Molecular and Optical Physics* 49.20 (2016), p. 202001.

[3] J. D. Whalen et al. “Probing nonlocal spatial correlations in quantum gases with ultra-long-range Rydberg molecules”. In: *Phys. Rev. A* 100 (1 2019), p. 011402.

[4] Hendrik Weimer et al. “Quantum critical behavior in strongly interacting Rydberg gases”. In: *Physical Review Letters* 101.25 (2008), p. 250601.

[5] Vera Bendkowsky et al. “Observation of ultralong-range Rydberg molecules”. In: *Nature* 458.7241 (2009), pp. 1005–1008.

[6] Simone Notarnicola, Mario Collura, and Simone Montangero. "Real-time-dynamics quantum simulation of (1+ 1)-dimensional lattice QED with Rydberg atoms". In: *Physical Review Research* 2.1 (2020), p. 013288.

[7] Thanh Long Nguyen et al. "Towards quantum simulation with circular Rydberg atoms". In: *Physical Review X* 8.1 (2018), p. 011032.

[8] FB Dunning et al. "Recent advances in Rydberg physics using alkaline-earth atoms". In: *Journal of Physics B: Atomic, Molecular and Optical Physics* 49.11 (2016), p. 112003.

[9] Thomas F Gallagher. *Rydberg atoms*. Vol. 3. Cambridge University Press, 2005.

[10] RF Stebbings, FB Dunning, et al. *Rydberg states of atoms and molecules*. Cambridge University Press, 1983.

[11] Thomas Amthor. "Interaction-Induced Dynamics in Ultracold Rydberg Gases–Mechanical Effects and Coherent Processes". PhD thesis. PhD thesis, Universität Freiburg, 2008.

[12] Brian Harold Bransden, Charles Jean Joachain, and Theodor J Plivier. *Physics of atoms and molecules*. Pearson education, 2003.

[13] Peter Van der Straten and Harold Metcalf. *Atoms and molecules interacting with light: Atomic physics for the laser era*. Cambridge University Press, 2016.

[14] W Neuhauser et al. "Localized visible Ba+ mono-ion oscillator". In: *Physical Review A* 22.3 (1980), p. 1137.

[15] Nicolas Schlosser et al. “Sub-poissonian loading of single atoms in a microscopic dipole trap”. In: *Nature* 411.6841 (2001), pp. 1024–1027.

[16] Peter Schauß et al. “Observation of spatially ordered structures in a two-dimensional Rydberg gas”. In: *Nature* 491.7422 (2012), pp. 87–91.

[17] Bruno Zimmermann et al. “High-resolution imaging of ultracold fermions in microscopically tailored optical potentials”. In: *New Journal of Physics* 13.4 (2011), p. 043007.

[18] Simon Stellmer et al. “Bose-Einstein condensation of strontium”. In: *Physical review letters* 103.20 (2009), p. 200401.

[19] Simon Stellmer et al. “Laser cooling to quantum degeneracy”. In: *Physical review letters* 110.26 (2013), p. 263003.

[20] Mumtaz Sheikh, Haad Yaqub Rathore, and Sohaib Abdul Rehman. “High-efficiency phase flattening based Laguerre–Gauss spectrometer using variable focus lenses”. In: *JOSA B* 34.1 (2017), pp. 76–81.

[21] Haad Yaqub Rathore et al. “High-efficiency measurement of all orbital angular momentum modes in a light beam”. In: *JOSA B* 34.7 (2017), pp. 1444–1449.

[22] Sonja Franke-Arnold et al. “Optical ferris wheel for ultracold atoms”. In: *Optics Express* 15.14 (2007), pp. 8619–8625.

[23] Sharon A Kennedy et al. “Confinement of ultracold atoms in a Laguerre–Gaussian laser beam created with diffractive optics”. In: *Optics Communications* 321 (2014), pp. 110–115.

[24] Philip PJ Zupancic. “Dynamic holography and beamshaping using digital micromirror devices”. MA thesis. Ludwig-Maximilians-Universitat Munchen, 2013.

[25] Joseph W Goodman. *Introduction to Fourier optics*. Ch:4. Roberts and Company Publishers, 2005.

[26] Justin Peatross and Michael Ware. *Physics of light and optics*. Ch:10. Brigham Young University, Department of Physics, 2011.

[27] A Lengwenus et al. “Coherent transport of atomic quantum states in a scalable shift register”. In: *Physical review letters* 105.17 (2010), p. 170502.

[28] Fabrice Merenda et al. “Miniaturized high-NA focusing-mirror multiple optical tweezers”. In: *Optics express* 15.10 (2007), pp. 6075–6086.

[29] Adrian Cheng et al. “Simultaneous two-photon calcium imaging at different depths with spatiotemporal multiplexing”. In: *Nature methods* 8.2 (2011), pp. 139–142.

[30] Daniel Petter. “Spatial modulation of light for ultracold gas experiments with erbium atoms”. MA thesis. University of Innsbruck, 2015.

[31] Philip Zupancic et al. “Ultra-precise holographic beam shaping for microscopic quantum control”. In: *Optics express* 24.13 (2016), pp. 13881–13893.

[32] G Gauthier et al. “Direct imaging of a digital-micromirror device for configurable microscopic optical potentials”. In: *Optica* 3.10 (2016), pp. 1136–1143.

[33] Mohammadamin Tajik et al. “Designing arbitrary one-dimensional potentials on an atom chip”. In: *Optics Express* 27.23 (2019), pp. 33474–33487.

[34] Anton Mazurenko et al. “A cold-atom Fermi–Hubbard antiferromagnet”. In: *Nature* 545.7655 (2017), pp. 462–466.

[35] *Handbook of LCOS SLM.* Ch:12. Hamamatsu Corporation.

[36] Takeshi Fukuhara et al. “Quantum dynamics of a mobile spin impurity”. In: *Nature Physics* 9.4 (2013), pp. 235–241.

[37] B. R. Brown and A. W. Lohmann. “Complex Spatial Filtering with Binary Masks”. In: *Appl. Opt.* 5.6 (June 1966), pp. 967–969.

[38] Sri Nivas Chandrasekaran et al. “Using digital micromirror devices for focusing light through turbid media”. In: *Emerging Digital Micromirror Device Based Systems and Applications VI.* Vol. 8979. International Society for Optics and Photonics. 2014, p. 897905.

[39] Donald B Conkey et al. “High-speed phase-control of wavefronts with binary amplitude DMD for light control through dynamic turbid media”. In: *MEMS Adaptive Optics VII.* Vol. 8617. International Society for Optics and Photonics. 2013, p. 86170I.

[40] Sergey Turtaev et al. “Comparison of nematic liquid-crystal and DMD based spatial light modulation in complex photonics”. In: *Optics express* 25.24 (2017), pp. 29874–29884.

[41] https://www.hamamatsu.com/us/en/product/type/X13138-04/index.html.

[42] Daniel Barredo et al. “Synthetic three-dimensional atomic structures assembled atom by atom”. In: *Nature* 561.7721 (2018), pp. 79–82.

[43] Florence Nogrette et al. “Single-atom trapping in holographic 2D arrays of microtraps with arbitrary geometries”. In: *Physical Review X* 4.2 (2014), p. 021034.

[44] Tingting Zeng et al. “Three-dimensional vectorial multifocal arrays created by pseudo-period encoding”. In: *Journal of Optics* 20.6 (2018), p. 065605.

[45] Changhe Zhou and Liren Liu. “Numerical study of Dammann array illuminators”. In: *Applied optics* 34.26 (1995), pp. 5961–5969.

[46] Pascuala García-Martínez et al. “Generation of Bessel beam arrays through Dammann gratings”. In: *Applied optics* 51.9 (2012), pp. 1375–1381.

[47] Ignacio Moreno et al. “Encoding generalized phase functions on Dammann gratings”. In: *Optics letters* 35.10 (2010), pp. 1536–1538.

[48] J Jahns et al. “Dammann gratings for laser beam shaping”. In: *Optical Engineering* 28.12 (1989), p. 281267.

[49] Rick L Morrison. “Symmetries that simplify the design of spot array phase gratings”. In: *JOSA A* 9.3 (1992), pp. 464–471.

[50] Susan J Walker and Jürgen Jahns. “Array generation with multilevel phase gratings”. In: *JOSA A* 7.8 (1990), pp. 1509–1513.

[51] Henning Labuhn et al. “Tunable two-dimensional arrays of single Rydberg atoms for realizing quantum Ising models”. In: *Nature* 534.7609 (2016), pp. 667–670.

[52] Hikaru Tamura et al. “Highly uniform holographic microtrap arrays for single atom trapping using a feedback optimization of in-trap fluorescence measurements”. In: *Optics express* 24.8 (2016), pp. 8132–8141.

[53] Graeme Whyte and Johannes Courtial. “Experimental demonstration of holographic three-dimensional light shaping using a Gerchberg–Saxton algorithm”. In: *New Journal of Physics* 7.1 (2005), p. 117.

[54] David Bowman et al. “High-fidelity phase and amplitude control of phase-only computer generated holograms using conjugate gradient minimisation”. In: *Optics express* 25.10 (2017), pp. 11692–11700.

[55] David Bowman. “Ultracold atoms in flexible holographics traps”. PhD thesis. University of St Andrews, 2018.

[56] T. A. Savard, K. M. O’Hara, and J. E. Thomas. “Laser-noise-induced heating in far-off resonance optical traps”. In: *Phys. Rev. A* 56 (2 Aug. 1997), R1095–R1098.

[57] Waseem S Bakr et al. “Probing the superfluid–to–Mott insulator transition at the single-atom level”. In: *Science* 329.5991 (2010), pp. 547–550.

[58] Antoine Browaeys, Daniel Barredo, and Thierry Lahaye. “Experimental investigations of dipole–dipole interactions between a few Rydberg atoms”. In: *Journal of Physics B: Atomic, Molecular and Optical Physics* 49.15 (2016), p. 152001.

[59] Harry Levine et al. “High-fidelity control and entanglement of rydberg-atom qubits”. In: *Physical review letters* 121.12 (2018), p. 123603.

[60] Carsten Robens et al. “High numerical aperture (NA= 0.92) objective lens for imaging and addressing of cold atoms”. In: *Optics letters* 42.6 (2017), pp. 1043–1046.

[61] Yvan RP Sortais et al. “Diffraction-limited optics for single-atom manipulation”. In: *Physical Review A* 75.1 (2007), p. 013406.

[62] Paul Yoder and Daniel Vukobratovich. *Opto-Mechanical Systems Design, Two Volume Set*. Crc Press, 2015.

[63] Rudolf Grimm, Matthias Weidemüller, and Yurii B Ovchinnikov. “Optical dipole traps for neutral atoms”. In: *arXiv preprint physics/9902072* (1999).

[64] Herman A Haus. “Mode-locking of lasers”. In: *IEEE Journal of Selected Topics in Quantum Electronics* 6.6 (2000), pp. 1173–1185.

[65] Harold J. Metcalf and Peter van der Straten. *Laser Cooling and Trapping*. Springer, New York, NY, 1999.

[66] Andrew Zangwill. *Modern electrodynamics*. Cambridge University Press, 2013.

[67] Pantazis Mouroulis, John Macdonald, and John Macdonald. *Geometrical optics and optical design*. Ch:4, Appendix. Oxford University Press New York, 1997.

[68] Adriaan Walther and A Walther. *The ray and wave theory of lenses*. Vol. 15. Cambridge University Press, 1995.

[69] *OSLO Optics Reference*. Lambda Research Corporation.

[70] Wolfgang Alt. “An objective lens for efficient fluorescence detection of single atoms”. In: *Optik* 113.3 (2002), pp. 142–144.

[71] Thomas G Kuper and Thomas I Harris. “Global optimization for lens design: an emerging technology”. In: *Lens and Optical Systems Design*. Vol. 1780. International Society for Optics and Photonics. 1993, p. 178003.

[72] J. D. Pritchard, J. A. Isaacs, and M. Saffman. “Long working distance objective lenses for single atom trapping and imaging”. In: *Review of Scientific Instruments* 87.7 (2016), p. 073107.

[73] L. M. Bennie et al. “A versatile high resolution objective for imaging quantum gases”. In: *Opt. Express* 21.7 (Apr. 2013), pp. 9011–9016.

[74] Francisco Camargo. “Rydberg Molecules and Polarons in Ultracold Strontium Gases”. PhD thesis. Rice University, 2017.

[75] Roger Ding. “Narrow line cooling of 84sr”. MA thesis. Rice University, 2016.